nature physics

LETTERS

PUBLISHED ONLINE: 21 SEPTEMBER 2015 | DOI: 10.1038/NPHYS3469

Propagating gene expression fronts in a one-dimensional coupled system of artificial cells

Alexandra M. Tayar[1†], Eyal Karzbrun[1†], Vincent Noireaux[2] and Roy H. Bar-Ziv[1*]

Living systems employ front propagation and spatiotemporal patterns encoded in biochemical reactions for communication, self-organization and computation[1–4]. Emulating such dynamics in minimal systems is important for understanding physical principles in living cells[5–8] and *in vitro*[9–14]. Here, we report a one-dimensional array of DNA compartments in a silicon chip as a coupled system of artificial cells, offering the means to implement reaction–diffusion dynamics by integrated genetic circuits and chip geometry. Using a bistable circuit we programmed a front of protein synthesis propagating in the array as a cascade of signal amplification and short-range diffusion. The front velocity is maximal at a saddle-node bifurcation from a bistable regime with travelling fronts to a monostable regime that is spatially homogeneous. Near the bifurcation the system exhibits large variability between compartments, providing a possible mechanism for population diversity. This demonstrates that on-chip integrated gene circuits are dynamical systems driving spatiotemporal patterns, cellular variability and symmetry breaking.

Sharp travelling fronts are prevalent in nature and emerge when nonlinear and dispersive effects combine, for example solitary waves in nonlinear optics, fluid convection, and chemical reactions[15]. Biological multicellular systems use travelling fronts of molecular signals as a means for computation and communication over long distances when signalling by diffusion is inefficient. In these systems, cells can be described as autocatalytic units that amplify and transmit signals beyond a threshold. Because signals dissipate in the medium over short distances, long-range information transmission is achieved by consecutive local cell–cell interactions. Signal propagation has been measured over orders of magnitudes in a variety of biological processes, ranging from fast action potentials in neuron networks with typical velocities[16] of $v \approx 10^7$ mm h^{-1}, to slow gene expression fronts in development[3] with $v \approx 0.1$ mm h^{-1}. Although some systems have a linearly unstable initial state, and thus can be treated as Fisher waves[17], the majority of biological examples require more complex models, including the cable equation and Hodgkin–Huxley model[18]. These systems raise questions concerning the selected speed, bifurcations, fluctuations and stability in parameter space[15], which are challenging to study in a living organism.

Front propagation has been extensively studied in chemical reactions[16,19] and more recently in reconstituted biological systems, including the bacterial cell division network[10], the *Xenopus laevis* cell cycle[11], and RNA (ref. 20) and DNA (ref. 14) catalytic reactions. In the past decade cell-free transcription–translation reactions have been used to advance the design of programmable artificial gene systems, including bulk solution[21], gels[9], membrane vesicles[22], water-in-oil drops[23], microfluidic devices[24] and on-chip DNA compartments[13]. So far, however, a synthetic spatially coupled cellular system, driven by integrated programmable gene expression circuits and capable of long-range communication, has not been reconstructed. Here, we used our recently developed on-chip DNA compartments[13] to design a one-dimensional array of coupled artificial cells programmed with a bistable genetic circuit to exhibit front propagation.

The array consisted of 15 compartments connected to a main flow channel and interconnected by fork-shaped capillaries. The array was carved in silicon to a shallow depth $h = 2$–3 μm, with compartment radius $R = 50$ μm, capillary lengths $L_1 = 150$ μm, $L_2 = 400$ μm, $L_3 = 50$ μm, and width $W = 10$ μm. The main flow channel was 50 μm deep and 900 μm wide (Fig. 1a and Supplementary Fig. 1). Gene circuits were patterned in every compartment, the device was sealed, and *Escherichia coli* cell extract continuously flowed through the main channel[13]. Protein synthesis initiated by diffusion of cell extract from the flow channel through the capillaries and into the compartments (Methods). Synthesized proteins were evacuated at the capillary opening to the flow channel, setting a boundary condition of zero protein concentration.

The expression–diffusion dynamics were characterized by a separation of timescales between the diffusion of proteins along the capillaries, which reached steady-state profiles within minutes, and the gene expression dynamics, which changed over hours[13] (Supplementary Information). Thus, we observed steady-state linear concentration gradients along the capillaries and a homogeneous protein concentration, p_i, within each compartment, $i = 1$–15, throughout the expression dynamics (Supplementary Fig. 2). The protein flux out of each compartment can be derived by Fick's law, $J = -D_0 \nabla p_i = -p_i/\tau$, setting a geometrically defined protein lifetime, $\tau = (\pi R^2 L_1 / D_0 W)\Phi_1(L_1/L_2, L_2/L_3) \approx 0.4$ h, where $D_0 \approx 0.126$ mm^2 h^{-1} (3.5×10^{-7} cm^2 s^{-1}) is the protein diffusion constant and $\Phi_1 \approx 0.5$ (Supplementary Equations 1–20). In general, $0 < \Phi_1 < 1$ depends on the inter-compartment connections, and for the case of isolated compartments $\Phi_1(L_2/L_1 \gg 1) = 1$ (Supplementary Equation 20).

The diffusion flux between compartments is determined by the fork-shaped capillaries, (L_2, L_3), and can be estimated by applying Kirchhoff current conservation law at each junction and Fick's law with a linear concentration gradient along the capillaries (Supplementary Equations 8–21). This leads to a discrete one-dimensional diffusion term for p_i in the ith compartment, $\Delta p_i = D((p_{i-1} + p_{i+1} - 2p_i)/L_2^2)$, with an effective diffusion coefficient, $D = D_0(L_2 W / \pi R^2)\Phi_2(L_2/L_3) \approx 0.02$ mm^2 h^{-1} and $\Phi_2 = 0.28$ (Supplementary Equation 21). For short shunts, $\Phi_2(L_3 \ll L_2) \to 0$, diffusion between compartments is negligible compared to diffusion to the main channel, which approached the limit of isolated compartments[13].

[1]Department of Materials and Interfaces, Weizmann Institute of Science, Rehovot 76100, Israel. [2]Department of Physics, University of Minnesota, Minneapolis, Minnesota 55455, USA. †These authors contributed equally to this work. *e-mail: roy.bar-ziv@weizmann.ac.il

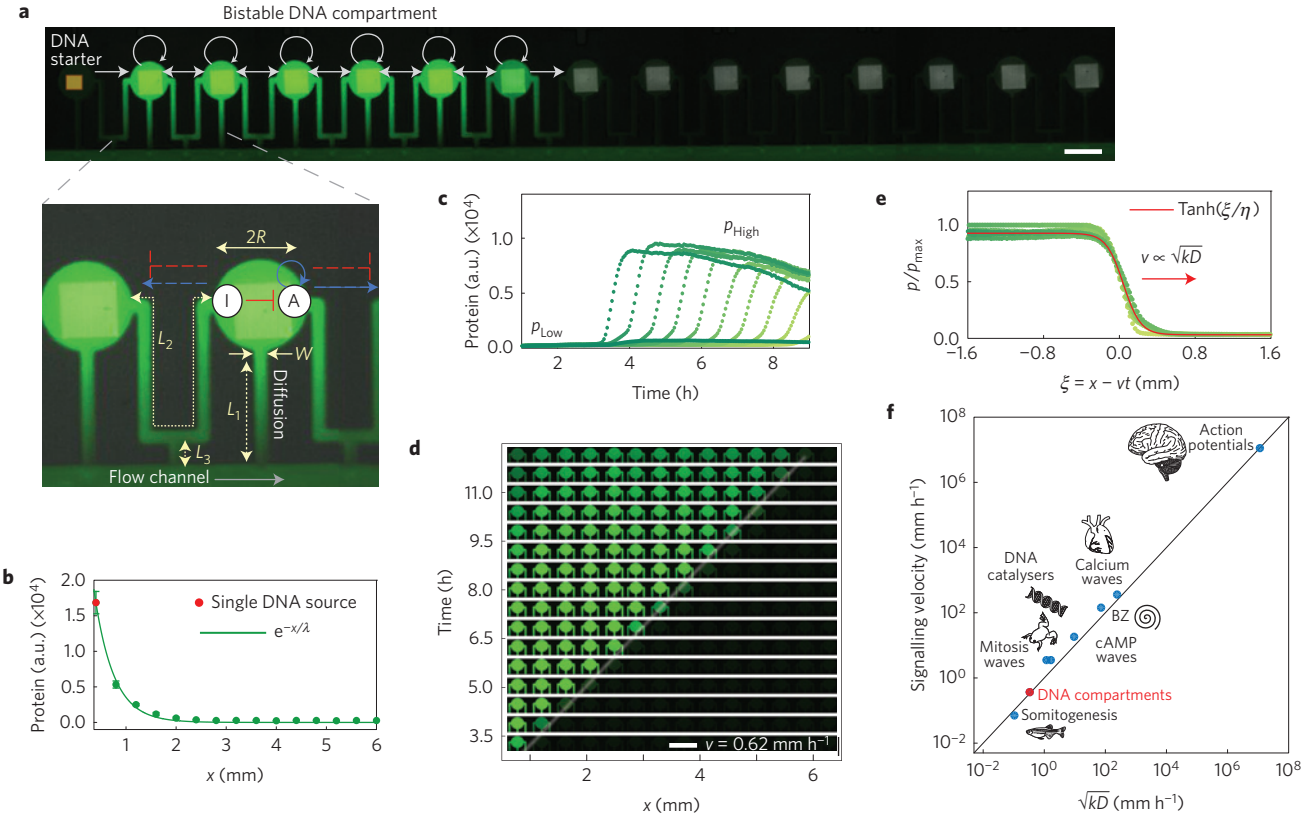

Figure 1 | Travelling gene expression front in an array of coupled DNA compartments. a, Overlay image of expressed GFP and fluorescently labelled DNA patterns (white squares). Compartments 2–15 (from left) were patterned with a bistable gene circuit; the first one patterned with a small amount of starter construct to initiate propagation. Scale bar, 100 μm. Inset: single compartment overlaid with the self-activator/inhibitor (A/I) scheme using activator σ^{28} and inhibitor Aσ^{28}. **b**, GFP concentration profile in arbitrary units (a.u.) along 15 compartments formed from a single DNA source in the first compartment. Solid line is an exponential fit, $e^{-x/\lambda}$, with $\lambda = 0.416 \pm 0.016$ mm (1.04 ± 0.04 compartments) averaged over 4 h of expression. **c**, Expression dynamics of the propagator during 9 h of experiment. Each graph represents the profile in a compartment according to their order in the array. **d**, A spacetime image of GFP in the array propagating at a constant velocity of $v = 0.62$ mm h^{-1} (1.55 compartment h^{-1}). **e**, Collapse of fronts in the travelling frame of reference, $\xi = x - vt$. Protein levels are normalized to the maximal protein value in the array for each time point (Supplementary Information). Red line is a fit to Tanh(ξ/η) with $\eta \approx 0.2$ mm (0.5 compartment). **f**, Propagation velocity for a range of biological systems as a function of scaling parameter $\sqrt{kD}$, where D is the diffusion constant of the propagating signal, and k is the typical autocatalytic rate of each system. The DNA compartment array is denoted in red. Exact range appears in Supplementary Table 1.

The diffusion between compartments, effective protein lifetime, and nonlinear interactions dictated by the genetic circuit can all be summarized in a discrete one-dimensional reaction–diffusion equation:

$$\partial_t p_i = \Delta p_i - \frac{p_i}{\tau} + f(p_i)$$

Here, $f(p_i)$ is the protein synthesis rate in response to the local protein concentration p_i, and is determined by the genetic circuit. The array was designed to obtain nearest-neighbour interactions, with a diffusion length smaller than a single compartment, $\sqrt{D\tau} \approx 0.1\,\text{mm} < L_2$, (Supplementary Equations 22–24). Indeed, we measured an exponentially decaying protein concentration gradient from a single DNA source with a decay length of $\lambda \approx 0.4$ mm (one compartment) along the array (Fig. 1b).

To program signal propagation we designed a bistable gene circuit comprising an activator in a self-feedback loop, and its inhibitor (Fig. 1a, inset, Supplementary Fig. 3)[25]. The circuit dynamics attained one of two steady-state protein expression levels reported using green fluorescent protein (GFP): high $p_{High} \approx 0.5$ μm, or p_{Low} of concentration lower than detection limit (≈50 nM; Supplementary Fig. 4). In the absence of the inhibitor a small leak initiates the positive feedback and the circuit dynamics has a single steady-state solution, p_{High}. The circuit is modelled accounting for the competition over gene expression machinery (Supplementary Equations 25–40), resulting in a circuit response function $f(p_i)$ for the activator dynamics, p_i, (Supplementary Equation 40). The bistable circuit was patterned in all compartments except for the anterior one, which was patterned with a 'starter' gene constantly expressing the activator at concentration lower than p_{High}.

During the first 3.5 h of expression all compartments maintained p_{Low} (Fig. 1c,d $t < 3.5$ h). Signalling was initiated from the anterior compartment, followed by diffusion of activator to the neighbouring compartment. This triggered the autocatalytic reaction, switching the neighbouring compartment to p_{High} at $t = 3.5$ h, and creating a new source of activator. The cycle of synthesis and diffusion propagated along the array at a constant velocity of $v = 0.62$ mm h^{-1} (1.55 compartment h^{-1} with compartment unit length $L_2 = 0.4$ mm; Fig. 1d). The expression dynamics in the array exhibited sequential switching to a high steady-state level, with a delay of $\Delta t \approx 0.7$ h between neighbouring compartments (Fig. 1c), and a gradual decrease in protein synthesis due to intrinsic decay in cell extract activity (Methods). In a moving frame of reference, $\xi = x - vt$, the spatiotemporal levels collapsed to a single step-function, Tanh((ξ/η)), with $\eta = 0.2$ mm (half a compartment; Fig. 1e). The front velocity is consistent with the scaling $v \propto \sqrt{kD} \approx 0.34$ mm h^{-1}. Here, $k \approx 5.4$ h^{-1} is the growth rate of the autocatalytic reaction estimated experimentally from the initial protein synthesis rate,

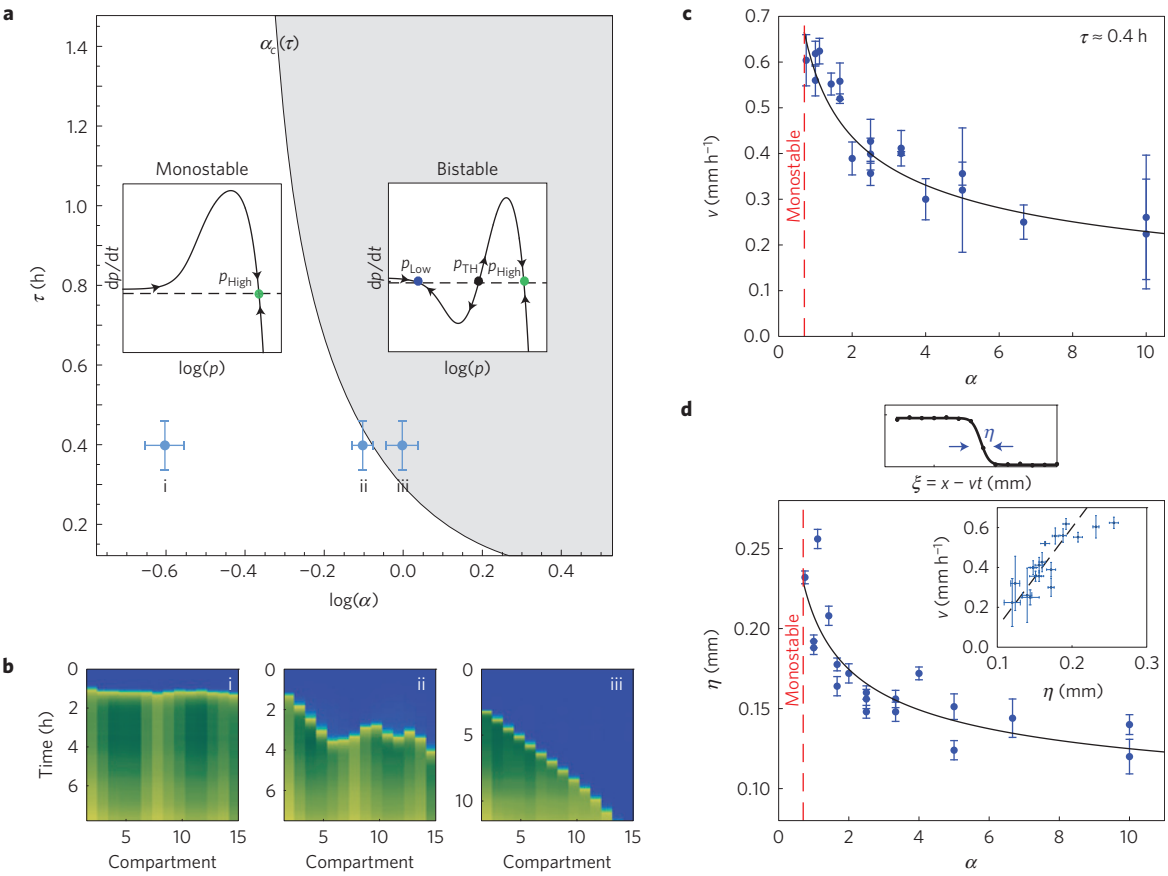

Figure 2 | Propagation dynamics regulated by gene circuit. a, A model-based phase diagram in parameter space of lifetime τ and gene ratio $\alpha = G_I/G_A$ showing a region of monostability with a single fixed point (left inset), and a region of bistability with two stable (p_{High} and p_{Low}) and one unstable (p_{TH}) fixed points (right inset). Error bars are estimated from variation in lifetime and gene ratio (Supplementary Fig. 7). Points labelled i–iii are described in **b**. **b**, Spacetime plots of propagator in the DNA array for the three points marked in **a** in the (i) monostable, (ii) close to transition and (iii) bistable regimes. Blue (green) colour represents low (high) protein level. **c**, Propagation velocity as a function of α. Plot shows three different experiments. Solid line is a fit to $v = v_0\alpha^{-\beta}$, $\beta = 0.4 \pm 0.07$, $v_0 = 0.59 \pm 0.02\,\mathrm{mm\,h^{-1}}$. Each data point is taken from a single experiment with front propagation over a number of compartments. The velocity is extracted by fitting a linear slope to the expression onset time in each compartment as a function of compartment location. The error bar is given by the velocity fit error for each experiment. **d**, Propagation front width η as a function of α, calculated from a fit of the collapsed and normalized propagating front. Solid line is a fit to $\eta = 0.07(1+2\alpha^{-0.4})$(mm). Inset: velocity as a function of front width; black line is a linear fit. Each data point is taken from a single experiment, and the error bar is given by the width fit error for each experiment.

$\partial_t p_i = kp_i$, which fits to an exponential growth with a rate k at low protein concentrations (Supplementary Fig. 5). This scaling, also known as Luther's formula[16], is common to autocatalytic reaction–diffusion systems in chemistry and biology, and has been observed over many orders of magnitude (Fig. 1f and Supplementary Table 1), including gene expression fronts propagating through the anteroposterior axis of developing vertebrates[26], mitosis waves in *Xenopus* eggs[11], cAMP waves spatial organization of amoeba[27], calcium waves in the heart[28], and action potentials in neurons[16]. The gene expression propagation velocity in the array is slower than *in vitro* enzymatic front waves[10,14,20] $v \approx 3\,\mathrm{mm\,h^{-1}}$, and chemical reactions such as Belousov–Zhabotinsky[16] $v \approx 140\,\mathrm{mm\,h^{-1}}$.

The theoretical model of the gene circuit, $f(p_i)$ (Supplementary Equation 40), revealed a transition from a bistable regime supporting front propagation to a monostable regime, which occurs along a saddle-node bifurcation line $\alpha_c(\tau)$ in the parameter space of protein lifetime, τ, and gene ratio, $\alpha = (G_I/G_A)$, of inhibitor and activator (Fig. 2a and Supplementary Fig. 6). The inhibitor gene concentration was fixed in theory and experiment. A bistable regime requires a high inhibitor concentration to suppress the autocatalytic leak, which corresponds to a long protein lifetime, or high gene ratio. A monostable regime is found at a low gene ratio, or short lifetime. In the bistable regime, $\alpha > \alpha(\tau)$, the activator flow chart exhibits two stable fixed points, corresponding to high and low protein levels (Fig. 2a, right inset). There is an additional unstable fixed point, p_{TH}, which is the concentration threshold for switching the compartment between the two expression states. In crossing the saddle-node bifurcation line, the two fixed points p_{TH} and p_{Low} are annihilated, and in the monostable regime, $\alpha < \alpha_c(\tau)$, there is a single fixed point of high levels p_{High} (Fig. 2a, left inset). Notably, the competition over gene expression machinery is not necessary to achieve bistability, but expands the bistable region in parameter space (Supplementary Fig. 6)[29].

We fabricated multiple arrays with identical lifetime $\tau \approx 0.4\,\mathrm{h}$, and different gene ratios $0.1 < \alpha < 10$, with 5–10% variation in lifetime and gene ratio[13] (Supplementary Fig. 7). We observed two distinct regimes, as predicted in the phase diagram. At low inhibitor ratio, $\alpha < 0.7$, expression initiated simultaneously in all the compartments and reached high levels without observable propagation, corresponding to the monostable regime (Fig. 2b(i)). For $0.7 < \alpha < 10$, we observed a travelling gene expression front (Fig. 2b(iii)). The compartments maintained low expression levels (p_{Low}) until triggered by the propagating activator, corresponding to the bistable regime. Near the transition line, $\alpha \approx 0.7$, we observed signal propagation for a finite time, after which expression initiated simultaneously in the entire array (Fig. 2b(ii)). This suggests the

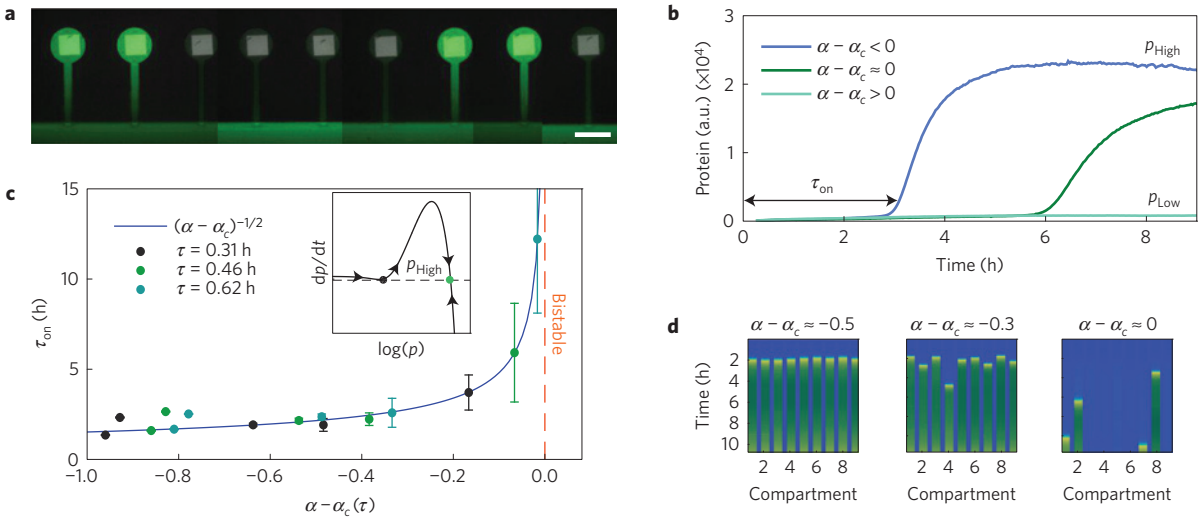

Figure 3 | Emergent fluctuations in single compartments near the transition. a, Overlay image of GFP and DNA in single compartments after 10 h of expression. The nine compartments were patterned with the bistable gene circuit at the same gene ratio α. Scale bar, 100 μm. **b**, Kinetics of the circuit in single compartments with $\tau = 1$ h for three different gene ratios. **c**, Reaction onset time in the compartments as a function of $\alpha - \alpha_c(\tau)$ for three different lifetimes. Each lifetime exhibited a different α_c, and the function was subtracted accordingly (Supplementary Information). Errors are taken from nine measurements for each point. Standard deviation increased up to 35% as the DNA ratio approached the transition to the bistable region $\alpha \to \alpha_c$. **d**, Spacetime plots showing nine repeats of single-compartment circuit kinetics, with $\tau = 0.62$ h, for three different gene ratios as denoted. Blue (green) colour represents low (high) protein level.

system is in the monostable regime, but exhibits long onset times. Our model implies a third regime for $\alpha > 10$, in which the system supports front propagation of p_{Low} into p_{High}. This is not observable because the initial state of the array is p_{Low} and there is a constant flux of activator proteins from the starter compartment (Supplementary Fig. 6).

We next explored the propagation velocity and front width as a function of gene ratio α in the bistable regime (Fig. 2c,d and Supplementary Fig. 8, $\alpha > 0.7$). At high inhibitor to activator gene ratio, $\alpha \gg \alpha_c$, the propagation was slow, $v\,(\alpha = 10) = 0.2\,\mathrm{mm\,h^{-1}}$. As we approached the bifurcation line, gene ratio in the compartment decreased, $\alpha \to \alpha_c$, positive feedback was triggered at lower activator concentration, and the velocity increased by a factor of three at $\alpha = 0.75$. Our model shows the threshold concentration is low near the bifurcation point, $p_{TH}\,(\alpha_c) \to p_{Low}$, hence compartments are easily excited to high activator levels, which is consistent with the observed faster propagation. The velocity is fitted with a power law, $v = v_0\alpha^{-\beta}$, with $\beta = 0.4 \pm 0.07$, $v_0 = 0.59 \pm 0.02\,\mathrm{mm\,h^{-1}}$ (Fig. 2c), which is close to the classical Luther scaling, $v = (Dk)^{\frac{1}{2}} \propto \alpha^{-\frac{1}{2}}$, where the autocatalytic growth rate is proportional to the activator gene concentration and inversely proportional to the gene ratio. The front width broadened with decreasing gene ratio α, but remained sharper than a compartment, $0.125 < \eta < 0.25\,\mathrm{mm}$ (Fig. 2d). The front width exhibited a linear dependence on the front velocity $\eta = \eta_0 + (v/k_0)$ (Fig. 2d), and $k_0 = 4.2\,\mathrm{h^{-1}}$ is close to the measured autocatalytic reaction rate, $5.4\,\mathrm{h^{-1}}$. This is consistent with the observed linear dependence, $\eta \propto v$, in other bistable models[18].

We next investigated the behaviour of the gene circuit in isolated compartments for varying lifetime τ and gene ratio α (Fig. 3a). We observed a transition between a monostable regime, $\alpha < \alpha_c$, in which the compartments spontaneously switched to high activator levels, and a bistable regime, $\alpha > \alpha_c$, in which the compartments remained at low levels (Fig. 3b), consistent with the propagation behaviour. The expression onset time in the monostable regime diverged near the bifurcation $\alpha_c\,(\tau)$, where the inhibition is sufficiently strong to prevent the onset of the positive feedback, beyond the duration of the experiment (~13 h; Fig. 3b,c). The transition point $\alpha_c(\tau)$ decreased with increasing lifetime τ, consistent with the phase diagram (Fig. 2a and Supplementary Figs 9 and 10). The divergence was consistent with a universal power-law scaling, $\tau_{on} \sim (\alpha - \alpha_c\,(\tau))^{-1/2}$, as expected near a saddle-node bifurcation[30]. Furthermore, we found a large variation in the expression onset time near the bifurcation (Fig. 3a,d and Supplementary Fig. 10). At $\alpha - \alpha_c = -0.5$ the expression onset time was $\tau_{on} = 2$ h, with less than 5% variation between compartments. Near the transition, $\alpha \approx \alpha_c$, the variation was greater than 35%, with only 40% of the compartments initiating expression in 13 h (Supplementary Fig. 11). The observed variation is surprising because the number of DNA copies in each compartment is large[13], ~10^7, and therefore stochastic effects should be negligible. However, the proximity to a transition point with diverging onset times amplifies small differences in gene ratio between compartments. This mechanism can play a crucial role in biological processes, such as development, which relies on spontaneous symmetry breaking[31]. To summarize, we have demonstrated front propagation of gene expression along an array of artificial cells using programmable integrated gene circuits. The spatial organization of DNA circuits together with short interaction length, set by the array geometry, will allow integrating long-range signalling with local information processing reactions based on gene expression, in analogy to multicellular systems, electronic circuits and neuronal networks.

Methods

Methods and any associated references are available in the online version of the paper.

Received 7 April 2015; accepted 10 August 2015; published online 21 September 2015

References

1. Gregor, T., Fujimoto, K., Masaki, N. & Sawai, S. The onset of collective behavior in social amoebae. *Science* **328,** 1021–1025 (2010).
2. Bassler, B. L. & Losick, R. Bacterially speaking. *Cell* **125,** 237–246 (2006).
3. Hubaud, A. & Pourquié, O. Signalling dynamics in vertebrate segmentation. *Nature Rev. Mol. Cell Biol.* **15,** 709–721 (2014).
4. Kandel, E., Schwartz, J., Jessell, T. M., Seigelbaum, S. A. & Hudspeth, A. J. *Principles of Neural Science* (McGraw-Hill Professional, 2012).
5. Bulter, T. *et al.* Design of artificial cell–cell communication using gene and metabolic networks. *Proc. Natl Acad. Sci. USA* **101,** 2299–2304 (2004).

6. Basu, S., Gerchman, Y., Collins, C. H., Arnold, F. H. & Weiss, R. A synthetic multicellular system for programmed pattern formation. *Nature* **434,** 1130–1134 (2005).
7. Matsuda, M., Koga, M., Nishida, E. & Ebisuya, M. Synthetic signal propagation through direct cell–cell interaction. *Sci. Signal.* **5,** ra31 (2012).
8. Danino, T., Mondragón-Palomino, O., Tsimring, L. & Hasty, J. A synchronized quorum of genetic clocks. *Nature* **463,** 326–330 (2010).
9. Isalan, M., Lemerle, C. & Serrano, L. Engineering gene networks to emulate *Drosophila* embryonic pattern formation. *PLoS Biol.* **3,** e64 (2005).
10. Loose, M., Fischer-Friedrich, E., Ries, J., Kruse, K. & Schwille, P. Spatial regulators for bacterial cell division self-organize into surface waves *in vitro*. *Science* **320,** 789–792 (2008).
11. Chang, J. B. & Ferrell, J. E. Mitotic trigger waves and the spatial coordination of the *Xenopus* cell cycle. *Nature* **500,** 603–607 (2013).
12. Keber, F. C. *et al.* Topology and dynamics of active nematic vesicles. *Science* **345,** 1135–1139 (2014).
13. Karzbrun, E., Tayar, A. M., Noireaux, V. & Bar-Ziv, R. H. Programmable on-chip DNA compartments as artificial cells. *Science* **345,** 829–832 (2014).
14. Zadorin, A. S., Rondelez, Y., Galas, J.-C. & Estevez-Torres, A. Synthesis of programmable reaction–diffusion fronts using DNA catalyzers. *Phys. Rev. Lett.* **114,** 068301 (2015).
15. Cross, M. & Hohenberg, P. Pattern formation outside of equilibrium. *Rev. Mod. Phys.* **65,** 851–1112 (1993).
16. Tyson, J. J. & Keener, J. P. Singular perturbation theory of traveling waves in excitable media (a review). *Physica D* **32,** 327–361 (1988).
17. Fisher, R. A. The wave of advance of advantageous genes. *Ann. Eugen.* **7,** 355–369 (1937).
18. Keener, J. P. & Sneyd, J. *Mathematical Physiology I* (Springer, 1998).
19. Winfree, A. T. Spiral waves of chemical activity. *Science* **175,** 634–636 (1972).
20. Bauer, G. J., McCaskill, J. S. & Otten, H. Traveling waves of *in vitro* evolving RNA. *Proc. Natl Acad. Sci. USA* **86,** 7937–7941 (1989).
21. Noireaux, V., Bar-Ziv, R. & Libchaber, A. Principles of cell-free genetic circuit assembly. *Proc. Natl Acad. Sci. USA* **100,** 12672–12677 (2003).
22. Noireaux, V. & Libchaber, A. A vesicle bioreactor as a step toward an artificial cell assembly. *Proc. Natl Acad. Sci. USA* **101,** 17669–17674 (2004).
23. Weitz, M. *et al.* Diversity in the dynamical behaviour of a compartmentalized programmable biochemical oscillator. *Nature Chem.* **6,** 295–302 (2014).
24. Niederholtmeyer, H., Stepanova, V. & Maerkl, S. J. Implementation of cell-free biological networks at steady state. *Proc. Natl Acad. Sci. USA* **110,** 15985–15990 (2013).
25. Kim, J., White, K. S. & Winfree, E. Construction of an *in vitro* bistable circuit from synthetic transcriptional switches. *Mol. Syst. Biol.* **2,** 68 (2006).
26. Bajard, L. *et al.* Wnt-regulated dynamics of positional information in zebrafish somitogenesis. *Development* **141,** 1381–1391 (2014).
27. Kessler, D. & Levine, H. Pattern formation in dictyostelium via the dynamics of cooperative biological entities. *Phys. Rev. E* **48,** 4801–4804 (1993).
28. Meyer, T. Cell signalling by second messenger waves. *Cell* **64,** 675–678 (1991).
29. Rondelez, Y. Competition for catalytic resources alters biological network dynamics. *Phys. Rev. Lett.* **108,** 018102 (2012).
30. Strogatz, S. H. *International Edition Nonlinear Dynamics and Chaos: With Applications to Physics, Biology, Chemestry and Engeneering* (Westview Press, 2001).
31. Artavanis-Tsakonas, S., Rand, M. D. & Lake, R. J. Notch signaling: Cell fate control and signal integration in development. *Science* **284,** 770–776 (1999).

Acknowledgements

We thank S. S. Daube for helpful discussions. V.N. thanks J. Garamella, R. Marshall and M. Rustad for technical help. This work was supported by: the Israel Science Foundation, the Minerva Foundation, and the Volkswagen Foundation (R.H.B.-Z.); the US–Israel Binational Science Foundation (R.H.B.-Z. and V.N.).

Author contributions

All authors contributed to all aspects of this work.

Additional information

Supplementary information is available in the online version of the paper. Reprints and permissions information is available online at www.nature.com/reprints. Correspondence and requests for materials should be addressed to R.H.B.-Z.

Competing financial interests

The authors declare no competing financial interests.

Methods

Biochip fabrication. The fabrication and assembly protocol of the DNA compartments is similar to previous work[13]. Each array was composed of 15 interconnected circular compartments etched 2.5–3 μm deep into a silicon wafer and connected to a main flow channel (Supplementary Fig. 1A). Silicon wafers (5″, 0.525 mm thickness, test grade, ⟨100⟩, p-type, University Wafers) were used as substrates. The compartments had a radius of 50 μm and were connected through a capillary channel, 10–15 μm in width to each other and to a perpendicular flow channel, 50 μm deep and 900 μm wide (Fig. 1a and Supplementary Fig. 1B). The flow channel had an inlet at one side and a 50-μm-wide serpentine ending with an outlet at the other side. The silicon wafer was patterned using standard lithography techniques (Photoresists S1818, AZ4562 MicroChem) and etched using reactive ion etching in an ICP-RIE (Surface Technology Systems) using the Bosch process[32] for deep features (>5 μm). The compartment and flow channel were etched in two separate steps. The inlets and outlets of each device were drilled using a drill machine (Proxxon, TBM 220). The device was cleaned using a base piranha solution followed by short incubation in hydrofluoric acid. The device was coated with a ∼50 nm SiO_2 layer deposited by low-temperature ALD (atomic layer deposition, FIJI F200, Cambridge Nanotech).

Biocompatible photoactivable monolayer assembly. The SiO_2-coated device was incubated with a biocompatible photoactivable polymer solution that self-assembled into a monolayer on the SiO_2 surface, for subsequent activation by ultraviolet light and binding of biomolecules[33]. The polymer is composed of a polyethylene glycol backbone with a Nvoc-protected amine at one end, and a trialkoxysilane function at the other end[33]. Incubation was carried for 20 min at 0.2 mg ml^{-1} in toluene, followed by rinsing in toluene and drying.

Lithography patterning for DNA assembly. The device was mounted on the translation stage of an inverted microscope (Zeiss Axiovert 200). Ultraviolet light from a fluorescent light source (EXFO X-Cite 120Q) was illuminated through a rectangular pinhole and a 365 nm band-pass filter (Chroma), and focused on the substrate using a ×60 objective. The exposure time was set to yield a total 2.5 J cm^{-2}. Reactive amine groups on the biocompatible photoactivable monolayer were exposed in surface patterns illuminated by ultraviolet light[33]. Biotin *N*-hydroxysuccinimidyl ester (biotin-NHS) dissolved in a borate buffered saline (0.5 mg ml^{-1}) was incubated on the chip for 15 min. The biotin-NHS covalently bound to the exposed amine groups on the exposed monolayer[33]. We thus attained a surface patterned with biotin.

DNA deposition and brush assembly. Linear DNA fragments were produced by polymerase chain reaction (PCR) with KAPA HiFi HotStart ReadyMix (KK2601, KAPA BIOSYSTEMS), using one primer with biotin and another with Alexa Fluor 647, both attached at the 5′-end (IDT). The biotin primer was located downstream of the transcription terminator. PCR products were cleaned using Promega Wizard SV-Gel and PCR Clean-Up. DNA was conjugated to streptavidin (SA) by mixing in solution in a molar ratio of 1:1.5 DNA:SA. The final DNA solution contained SA-conjugated DNA at a concentration of 100–300 nM in phosphate buffered saline (PBS).

Nanolitre DNA–SA droplets were individually deposited onto the reactor chambers using the GIX Microplotter II (Sonoplot) and 60-μm-diameter micropipettes. The DNA–SA solutions were incubated on the device for 1–2 h in PBS. During incubation the DNA formed a dense brush on the surface. The brush density was of the order of 10^3 DNA μm^{-2} (refs 33,34). The promoter orientation of the DNA was towards the surface of the DNA brush[35]. The gene size varied in the range 700–1,500 bp. The distance between the DNA top and the promoter is about 100–200 bp and a similar distance between the terminator and the DNA end attached to the surface. Finally, DNA brushes were localized to the lithographically patterned areas inside the etched compartments (Fig. 1a and Supplementary Fig. 1). The device was then bathed in PBS, and then in water to remove excess adsorbed DNA. The device was then gently dried with nitrogen.

All *E. coli* cell-free transcription–translation reaction (CFE). In this study we used a CFE that is a cytoplasmic extract from *E. coli* strain BL21 Rosetta2 (Novagen) according to a procedure described previously[36]. The cell-free reactions were composed of 33% (volume) crude extract and 66% (volume) of water, DNA and buffer with the following final composition: 50 mM HEPES pH 8, 1.5 mM ATP, 1.5 mM GTP, 0.9 mM CTP, 0.9 mM UTP, 0.2 mg ml^{-1} tRNA, 0.26 mM coenzyme A, 0.33 mM NAD, 0.75 mM cAMP, 0.068 mM folinic acid, 1 mM spermidine, 30 mM 3-phosphoglyceric acid, 2 mM DTT, 1.5 mM amino acids, 6.5 mM Mg-glutamate, 100 mM K-glutamate and 2% PEG 8000. During extract preparation, the endogenous DNA and mRNA were degraded. The cell extract provided the transcription and the translation machineries necessary for gene expression. Transcription was driven by the endogenous *E. coli* RNA polymerase and thus allowed us to use the entire repertoire of the *E. coli* regulation toolbox[37,38]. The CFE contained active proteases and ribonucleases. Previously, we studied the stability of proteins and mRNA in our cell-free system[13,36,39]. Proteins without a degradation tag were stable with no observed degradation. The protein GamS, was added to all of the reactions at a concentration of 3 μM to minimize the degradation of linear DNA by the 3′ exonuclease activity of the RecBCD complex[40] which was present in the CFE. The CFE was supplemented with 3-phosphoglyceric acid (3-PGA) for ATP regeneration[36]. The 3-PGA is a natural substrate to *E. coli* and therefore no enzyme was added to the extract.

Sealing the device and flow of CFE. The carved side of the device was sealed with a PDMS-coated glass coverslip and magnets. Magnets embedded in a punched PDMS were attached to the backside of the device (the untreated side of the device), aligned to the drilled inlet and outlet. The device inlet was connected using elastic tubing to a reservoir of PBS cooled to 2–4 °C with a cooling circulator (Huber ministat). The outlet was connected to a syringe pump (Harvard Apparatus Pico Plus). The device was placed on a microscope, in an incubating chamber (30 °C). Once the syringe pump was turned on, vacuum was applied and PBS flowed into the main flow channel and entered by capillarity into the compartments within a minute, pushing out air through the PDMS. The experiment began by exchanging PBS with CFE flowing in the main channel at a rate of ∼0.2 μl min^{-1} and diffusing through the thin capillaries into DNA compartments. Constant flow was maintained during the experiment, which was carried on for 12–15 h. During this long period there is a slow loss of extract activity, which is observed in a decaying expression envelope for all of the compartments.

Imaging. Cell-free expressed GFP in the compartments was imaged on an inverted microscope (Zeiss Axiovert 200) equipped with an automated translation stage, a sensitive wide view camera (ANDOR Neo sCMOS, Andor Technology) through a ×10 objective (Zeiss), and fluorescent excitation (Hg-illumination lamp (X-Cite 120) through a GFP filter set (488 nM).

Gene circuit design and assembly. DNA constructs used in this work are described in Supplementary Table 2. Their assembly into single gene constructs and gene networks is described in Supplementary Table 3, as well as in Supplementary Fig. 3. All the plasmids were constructed from the pBEST-Luc plasmid (Promega), with the UTR1 (untranslated region). DNA constructs (promoter gene) were assembled *in vitro* by PCR using a primer coding for the promoter and a plasmid template coding for the gene. This was followed by a second PCR with biotinylated primers and primers with Alexa Fluor 647, as previously described.

The bistable gene circuit (Fig. 1a inset, Supplementary Fig. 3 and Supplementary Tables 2–3) was constructed using an autocatalytic element and its inhibitor[25,41–44]:

Activator (P): $P_{28} - \sigma^{28}$, autocatalytic construct expressing the sigma-28 transcription factor[37] under its own promoter, P_{28}, thereby forming a positive feedback loop.

Inhibitor (I): $P_{70} - A\sigma^{28}$, constitutively expressing the anti-sigma factor 28, (FlgM; ref. 45) under a σ^{70} promoter[37]. The anti-sigma protein binds the sigma transcription factor with high affinity and forms a complex (**C**), and thus sequesters the binding of sigma-28 to its prompter, inhibiting the positive feedback.

In the experiment the gene ratio $\alpha = (G_I/G_P)$ of inhibitor G_I and autocatalytic G_P elements of the circuit were varied (Supplementary Fig. 3). The inhibitor and reporter constructs were kept at a constant concentration while the activator concentration was changed. To maintain the total DNA of each brush constant we used a non-coding 'dummy' DNA of the same length and concentration as the activator construct.

References

32. Wang, X., Zeng, W., Lu, G., Russo, O. L. & Eisenbraun, E. High aspect ratio Bosch etching of sub-0.25 μm trenches for hyperintegration applications. *J. Vac. Sci. Technol. B* **25,** 1376–1381 (2007).
33. Buxboim, A. *et al.* A single-step photolithographic interface for cell-free gene expression and active biochips. *Small* **3,** 500–510 (2007).
34. Bracha, D., Karzbrun, E., Shemer, G., Pincus, P. A. & Bar-Ziv, R. H. Entropy-driven collective interactions in DNA brushes on a biochip. *Proc. Natl Acad. Sci. USA* **110,** 4534–4538 (2013).
35. Daube, S. S., Bracha, D., Buxboim, A. & Bar-Ziv, R. H. Compartmentalization by directional gene expression. *Proc. Natl Acad. Sci. USA* **107,** 2836–2841 (2010).
36. Shin, J. & Noireaux, V. Efficient cell-free expression with the endogenous *E. coli* RNA polymerase and sigma factor 70. *J. Biol. Eng.* **4,** 8 (2010).
37. Shin, J. & Noireaux, V. An *E. coli* cell-free expression toolbox: Application to synthetic gene circuits and artificial cells. *ACS Synth. Biol.* **1,** 29–41 (2012).
38. Caschera, F. & Noireaux, V. Synthesis of 2.3 mg/ml of protein with an all *Escherichia coli* cell-free transcription–translation system. *Biochimie* **99,** 162–168 (2014).

39. Karzbrun, E., Shin, J., Bar-Ziv, R. H. & Noireaux, V. Coarse-grained dynamics of protein synthesis in a cell-free system. *Phys. Rev. Lett.* **106,** 048104 (2011).
40. Karu, A. E., Sakaki, Y., Echols, H. & Linn, S. The γ protein specified by bacteriophage γ. Structure and inhibitory activity for the recBC enzyme of *Escherichia coli*. *J. Biol. Chem.* **250,** 7377–7387 (1975).
41. Ferrell, J. E. Tripping the switch fantastic: How a protein kinase cascade can convert graded inputs into switch-like outputs. *Trends Biochem. Sci.* **21,** 460–466 (1996).
42. Gardner, T. S., Cantor, C. R. & Collins, J. J. Construction of a genetic toggle switch in *Escherichia coli*. *Nature* **403,** 339–342 (2000).
43. Chang, D.-E. *et al.* Building biological memory by linking positive feedback loops. *Proc. Natl Acad. Sci. USA* **107,** 175–180 (2010).
44. Huang, D., Holtz, W. J. & Maharbiz, M. M. A genetic bistable switch utilizing nonlinear protein degradation. *J. Biol. Eng.* **6,** 9 (2012).
45. Hughes, K. T. & Mathee, K. The anti-sigma factors. *Annu. Rev. Microbiol.* **52,** 231–286 (1998).

nature physics

SUPPLEMENTARY INFORMATION

DOI: 10.1038/NPHYS3469

Propagating gene expression fronts in a one-dimensional coupled system of artificial cells

DOI: 10.1038/NPHYS3469

Table of Contents

DOI: 10.1038/NPHYS3469

Supplementary Text

DNA Compartment theory

Single Compartment Lifetime

The derivation of the gene expression dynamics in a single compartment was previously published and is summarized here for clarity[13]. The synthesis of protein in the circular compartment is a slower process than diffusion across the compartment and capillary: With $L = 150\mu m$, $D_0 = 35\mu m^2/s$, $T_{diff} = L^2/2D = 5min$, whereas the time scale to reach steady-state protein synthesis $T_p \approx 1hr$ (Fig. S2). This separation of time scales allows us to use a steady-state approximation, in which the concentration of protein is homogenous in the compartment, and the diffusion along the capillary is at steady-state. The protein concentration $p(t, y)$ follows a 1D diffusion equation along the capillary $0 < y < L$,

$$\partial_t p = D_0 \partial_y^2 p, \tag{1}$$

with a boundary condition at the main flow channel $p(y = L) = 0$. At the compartment opening, $y = 0$, the protein concentration is equal to that within the compartment $p(y = 0) = p_c(t)$, which is the slow variable of interest. Thus, the concentration drop is linear along the capillary. We have previously shown[13] that the diffusion dynamics along the capillary is

$$p = p_C(t) \cdot \left(1 - \frac{y}{L}\right), \tag{2}$$

$$\partial_y p = -\frac{p_C(t)}{L}, \tag{3}$$

as measured (Fig S2). Within the compartment protein is synthesized at rate, a_{syn} and diffuses out of the compartment at a flux, J_{out}. The protein dynamics in the compartment is thus,

$$\partial_t p_C = a_{syn} + J_{out}. \tag{4}$$

From Fick's law the diffusion flux out of the compartment is:

$$J_{out} = \frac{D_0 A}{V} \partial_y p\big|_{y=0}. \tag{5}$$

Here we used the compartment volume $V = \pi R^2 h$ and compartment opening area $A = hW$. The channel and compartment height is h, the compartment radius is R, and the opening width is W. We thus obtain a first-order differential equation for the protein dynamics in the compartment,

$$\partial_t p_C = a_{syn} - \frac{p_C}{\tau}, \tag{6}$$

with effective protein lifetime in the compartment,

$$\tau = \frac{\pi R^2}{D_0 W} L. \tag{7}$$

For a compartment with the parameters $L = 150\mu m$, $W = 10\mu m$, $R = 50\mu m$ the lifetime is $\tau = 0.9hr$ consistent with the kinetics of the protein in the compartment (Fig S2) and longer than the diffusion time scale $\tau_D = 5min$ thus proving the validity of the steady-state approximation above.

One Dimensional array of compartments, effective lifetime and diffusion

Next, we consider an array of circular compartments interconnected through small capillaries (Fig. 1A, S1A, S12). Proteins synthesized in the compartments diffuse to the main flow channel through capillaries with width W_1 and length L_1 (red lines, Fig S12), setting the turnover mechanism described in the previous section. Proteins diffuse between compartments along capillaries of width W_2 and length L_2 (blue lines, Fig. S12). These capillaries are also connected to the main channel through shunts of width W_3 and length L_3(black lines, Fig. S12). In this section we show how the protein dynamics in the array can be described as an effective one-dimensional diffusion-reaction equation.

The protein dynamics in the $i's$ compartment is composed of diffusion flux of proteins from and to shunts $j-1$ and j, and to the main channel (Fig. S12),

$$\partial_t p_i = J_{j-1,i} + J_{j,i} - \frac{D_0 W_1}{\pi R^2 L_1} p_i \,. \tag{8}$$

As in previous section, we assume the dynamics along all capillaries is faster than in the compartment, hence we use the steady-state linear concentration gradients and Fick's law to derive the protein diffusion flux,

$$\partial_t p_i = \frac{D_0 W_2}{\pi R^2 (L_2/2)} \left(p_{j-1} - p_i\right) + \frac{D_0 W_2}{\pi R^2 (L_2/2)} \left(p_j - p_i\right) - \frac{D_0 W_1}{\pi R^2 L_1} p_i \,, \tag{9}$$

$$\partial_t p_i = \frac{2 D_0 W_2}{\pi R^2 L_2} \left(p_{j-1} + p_j - 2p_i\right) - \frac{D_0 W_1}{\pi R^2 L_1} p_i. \tag{10}$$

To determine p_{j-1} we use Kirchhoff current conservation law at junction j-1,

$$0 = D_0 W_2 h \left[\frac{p_{i-1} - p_{j-1}}{\frac{L_2}{2}} + \frac{p_i - p_{j-1}}{\frac{L_2}{2}} + \frac{0 - p_{j-1}}{\frac{L_3 W_2}{W_3}} \right]. \tag{11}$$

DOI: 10.1038/NPHYS3469

We find,

$$p_{j-1} = \frac{1}{2}\frac{p_{i-1}+p_i}{1+\frac{L_2 W_3}{4L_3 W_2}}. \tag{12}$$

We now define the geometrical ratio $\theta_2 = \frac{L_2 W_3}{L_3 W_2}$, which determines the diffusion flux through the shunt,

$$p_{j-1} = \frac{1}{2}\frac{p_{i-1}+p_i}{\left(1+\frac{\theta_2}{4}\right)} = \begin{cases} \frac{1}{2}(p_{i-1}+p_i) & \theta_2 \ll 1 \\ \frac{2}{\theta_2}(p_{i-1}+p_i) & \theta_2 \gg 1 \end{cases} \tag{13}$$

At the limit of very long and thin shunt $\theta_2 \ll 1$ the flux through the shunt is negligible and the concentration at the junction $j-1$ is the average of the two adjacent compartments. At the limit of very short and wide shunt $\theta_2 \gg 1$, the diffusion between compartments is negligible compared with diffusion out to the main channel through the shunt and $p_{j-1} \to 0$.

Using eq. (10) and (13) we find,

$$\partial_t p_i = \frac{2D_0 W_2}{\pi R^2 L_2}\left(\frac{1}{2}\frac{p_{i-1}+p_i}{1+\frac{\theta_2}{4}} + \frac{1}{2}\frac{p_{i+1}+p_i}{1+\frac{\theta_2}{4}} - 2p_i\right) - \frac{D_0 W_1}{\pi R^2 L_1}p_i. \tag{14}$$

We define two time scales $\tau_y = \frac{\pi R^2 L_1}{D_0 W_1}$, $\tau_x = \frac{\pi R^2 L_2}{D_0 W_2}$. The effective lifetime τ_y as in an isolated compartment, and τ_x is the diffusion time between two compartments in a system with no shunt.

$$\partial_t p_i = \frac{2}{\tau_x}\left(\frac{1}{2}\frac{p_{i-1}+p_i}{1+\frac{\theta_2}{4}} + \frac{1}{2}\frac{p_{i+1}+p_i}{1+\frac{\theta_2}{4}} - 2p_i\right) - \frac{p_i}{\tau_y} \tag{15}$$

$$\partial_t p_i = \frac{1}{\tau_x}\frac{1}{1+\theta_2/4}(p_{i-1}+p_{i+1}-2p_i) - \left[\frac{4}{\tau_x}\left(1-\frac{1}{1+\frac{\theta_2}{4}}\right)+\frac{1}{\tau_y}\right]p_i \tag{16}$$

We obtained a discrete 1D diffusion equation with an effective diffusion constant D and an effective lifetime τ.

$$\partial_t p_i = D\frac{(p_{i-1}+p_{i+1}-2p_i)}{L_2^2} - \frac{p_i}{\tau} \tag{17}$$

$$D = \frac{L_2^2}{\tau_x}\frac{1}{1+\theta_2/4} \tag{18}$$

$$\tau = \tau_y \left(1 + 4\theta_1 (1 - \frac{1}{1 + \frac{\theta_2}{4}}) \right)^{-1} \quad (19)$$

with a geometrical ratio $\theta_1 = \frac{\tau_y}{\tau_x} = \frac{L_1 W_2}{L_2 W_1}$. At the limit of a system with no shunt, $\theta_2 \to 0$, we find $D = d^2/\tau_x$ and $\tau = \tau_y$ as previously published[13]. In the opposite limit, $\theta_2 \gg 1$, the diffusion between compartments is small, $D \sim \frac{1}{\theta_2} \to 0$, and the lifetime in the compartment has a finite correction $\tau = \tau_y/(1 + 4\theta_1)$. We conclude that the shunt enables control over effective diffusion in the system with small effects over protein lifetime.

For example we calculate the effect of the shunt on the lifetime of the array shown in Fig 1,

No shunt	With shunt
$L_1 = 150\mu m$ $L_2 = 400\mu m$ $W_1 = W_2 = 12\mu m$ $W_3 = 0$ $D_0 = 0.126 mm^2/hr$ $(35\mu m^2/s)$	$L_1 = 150\mu m$ $L_2 = 400\mu m$ $L_3 = 40\mu m$ $W_1 = W_2 = 12\mu m$ $W_3 = 12\mu m$ $D_0 = 0.126 mm^2/hr$
$\tau \approx 0.8$ hr	$\tau \approx 0.4$ hr
$D = 0.075 mm^2/hr$	$D = 0.021 mm^2/hr$

Note that in the main text we refer to the lifetime and effective diffusion using functions of the geometry Φ_1 and Φ_2 which are defined here,

$$\Phi_1 \equiv \left(1 + 4\theta_1 (1 - \frac{1}{1 + \frac{\theta_2}{4}}) \right)^{-1} \quad (20)$$

$$\Phi_2 \equiv \frac{1}{1 + \theta_2/4} \quad (21)$$

In the continuum limit, $x = L_2 \cdot i, p_i \to p(x)$, we obtain a 1D reaction-diffusion equation,

$$\partial_t p = D \partial_x^2 p - \frac{p}{\tau} + f(p). \quad (22)$$

Here $f(p)$ is a programmable cellular response function.

DOI: 10.1038/NPHYS3469

For an array with a localized single DNA source the steady state protein concentration is an exponential decaying profile:

$$p(x) = p_0 e^{-\frac{x}{\lambda}}, \tag{23}$$

$$\lambda = \sqrt{D\tau}, \tag{24}$$

The theoretical decay length for our system ($D = 0.021\text{mm}^2/\text{hr},\ \tau = 0.4\text{hr}$) is $\lambda \approx 0.1\text{mm} = L_2/4$ and the measured decay length (Fig. 1B,S13) is $\lambda \approx 0.4\text{mm} = L_2$. The discrepancy results from: (i) The exponential solution only holds for $\lambda \gg L_2$, since the concentration profile between compartments is linear. (ii) The measurement was obtained for a DNA source in the first compartment with only one shunt connection and the theory is derived for an infinite array.

Inhibitor-Autocatalytic Bistable Network Analysis

Network dynamics

The bistable gene circuit (Fig. 1A inset, Fig. S3, Table S2-S3) was constructed using an autocatalytic element, $P_{28} - \sigma^{28}$ $(\boldsymbol{p})$, and its inhibitor, $P_{70} - A\sigma^{28}$ $(\boldsymbol{I})$ [25,41–44]. The anti-sigma protein binds the sigma transcription factor with high affinity and forms a complex $(\boldsymbol{C})$**,** and thus sequesters the binding of sigma-28 to its prompter, inhibiting the positive feedback**.** The sigma factor σ^{70} was endogenously present in the cell-free extract (CFE)[36,37,39], leading to constitutive expression of the inhibitor as well as a leak from the activator promoter P_{28}. We model the network dynamics in the following equations:

$$p + I \underset{k_{off}}{\overset{k_{on}}{\leftrightharpoons}} C$$

$$\partial_t p = k_p \cdot \left(\epsilon + \frac{p}{p + k_{28}}\right) - \frac{p}{\tau} - k_{on} p \cdot I + k_{off} C \tag{25}$$

$$\partial_t I = k_I - \frac{I}{\tau} - k_{on} p \cdot I + k_{off} C \tag{26}$$

$$\partial_t C = -\frac{C}{\tau} + k_{on} p \cdot I - k_{off} C \tag{27}$$

The parameters are: k_A synthesis rate of activator, k_I Synthesis rates of inhibitor, ϵ synthesis leak of the autocatalytic construct, k_{28} Michaelis-Menten (MM) constant for binding of the activator to its promoter P_{28}, τ Lifetime of proteins in the compartment, k_{on} binding rate of activator and inhibitor, k_{off} disassociation rate of activator and inhibitor. In eq. (25), the first term is the autocatalytic expression and leak, the second term is protein turnover and last two terms are binding and unbinding to inhibitor I. In eq. (26) the first term is the constitutive expression of the inhibitor; the second term is inhibitor turnover, and the last two terms as in eq. (25). In eq. (27) the first term is the complex turnover, and the last two terms as in eq. (25).

In our analysis we neglect mRNA dynamics and assume mRNA is localized in the DNA compartment. The mRNA is biochemically degraded in the CFE within $\tau_m \approx 5\text{min}$, and diffuses slowly compared to the protein $D_m < 10\mu\text{m}^2/\text{s}$ (0.036mm/hr) Thus, we estimate mRNA must be localized to a distance $l_m = \sqrt{D_m \tau_m} \approx 50\mu\text{m}$ of the DNA, which is smaller than compartment size. The mRNA transcription time provides an additional delay in the synthesis kinetics that may be important for understanding oscillatory dynamics.

We consider the scenario of front propagation in the array and make two simplifying assumptions:
1. The Inhibitor construct is constitutively expressing I in all of the compartments and reaches a steady-state concentration, $I_0 = k_I \tau \approx 1\mu\text{M}$ at about 1hr, before the activator p front wave initiates at $t > 3\text{hr}$; this is for $\tau \approx 0.4\text{hr}$ and $k_I = 2 - 2.5\mu\text{M/hr}$ (Table S4). Thus, we assume the total concentration of inhibitor is constant during the experiment.

$$\partial_t I_0 = \partial_t (I + C) = 0. \tag{28}$$

Removing this assumption will not affect the phase diagram, but the propagation kinetics will have two coupled equations for the activator and inhibitor.

2. The kinetics of the complex concentration C is dominated by binding and unbinding of inhibitor and activator, which occurs at fast time scales, $(k_{on} I_0)^{-1} \approx$ 2min ($k_{on} = 7\ \text{nM}^{-1}\text{s}^{-1}$,Table S4), compared with the accumulation of activator levels in the compartment which occurs over $\tau \approx 0.4\text{hr}$. We thus assume that the complex C is always at steady-state with respect to the free activator concentration,

$$\partial_t C = 0, \tag{29}$$

and using eq (27),

$$k_{on} p \cdot I - k_{off} C - \frac{C}{\tau} = 0, \tag{30}$$

$$C = \frac{I \cdot p}{k_d}, \tag{31}$$

where we defined the effective complex disassociation constant, $k_d = \frac{k_{off} + \frac{1}{\tau}}{k_{on}}$.

Use equations (31) and (28) in (26):

$$\partial_t I = 0, \tag{32}$$

$$k_I - \frac{I}{\tau} - k_{on} p \cdot I + k_{off} \cdot \frac{I \cdot p}{k_d} = 0, \tag{33}$$

$$I = \frac{k_I}{\tau^{-1} + (k_{on} - \frac{k_{off}}{k_d}) p} = \frac{k_I \tau}{1 + \frac{p}{k_d}}. \tag{34}$$

DOI: 10.1038/NPHYS3469

Using equations (34) and (31) back in (25) we find an effective equation for the activator dynamics,

$$\partial_t p = k_p \cdot [\epsilon + \frac{p}{k_{28}+p} - \frac{p}{k_p \tau} - \alpha \frac{p}{k_d + p}] \tag{35}$$

The first term is the synthesis leak, the second term is the positive feedback, the third term is the protein turn over and the last term is inhibition. The synthesis rate ratio $\alpha = \frac{k_I}{K_p}$ is proportional to the DNA ratio in each compartment, $\alpha \propto \frac{G_I}{G_p}$.

Network dynamics with competition over RNA polymerase

Previous work have shown that for a network of reactions where an enzyme (RNA polymerase R_p) is shared by more than one substrate (sigma factors σ^i) the different substrates competitively inhibit each other[29,37]. The Michaelis-Menten binding equilibrium then becomes:

$$[R_p \sigma^i] = R_p \frac{\sigma^i}{k_i(1 + \sum_j \sigma^j / k_j)} \tag{36}$$

with k_i the Michaelis-Menten constant for binding to the enzyme. The corresponding synthesis rates of protein x^i under control of sigma factor σ^i is

$$\partial_t x^i = V_i [R_p \sigma^i] \tag{37}$$

Here V_i is the synthesis rate constant. In the cell-free system used in this work the transcription factor concentrations can exceed the RNA Polymerase concentration $R_p \approx 100\text{nM}$[39] and therefore different transcription factors can competitively inhibit each other. The endogenous concentration transcription factor σ^{70} in the reaction is constant $\sigma^{70} \approx 30\text{nM}$[37], while σ^{28} is expressed from the autocatalytic construct. We thus use eq. (37) to write MM equations for competitive binding of σ^{28} (activator -A) and σ^{70} to the R_p.

	Without competition	With competition
$\partial_t p\|_{synthesis} = V_A[R_p p]$	$V_{28} \frac{pR_p}{k_{28}+p} = k_p \frac{p}{k_{28}+p}$	$V_{28} \frac{pR_p}{k_{28}+p+k_{28}\frac{\sigma^{70}}{k_{70}}} = k_p \frac{p}{k_{28}{}' + p}$
$\partial_t I\|_{synthesis} = V_{70}[R_p \sigma^{70}]$	$V_{70} \frac{R_p \sigma^{70}}{k_{70}+\sigma^{70}} = k_I$	$V_{70} \frac{R_p \sigma^{70}}{k_{70}+\sigma^{70}+\frac{p k_{28}}{k_{70}}} = \frac{k_I}{1+p/k_{comp}}$

Here we defined $k_p = V_{28} R_p$, and $k'_{28} = \frac{\sigma^{70} k_{70}}{k_{28}} + k_{28}$, $k_{comp} = \frac{k_{70}(k_{70}+\sigma^{70})}{k_{28}}$.

We thus get a modified equation for the activator p,

$$\partial_t p = k_p \cdot [\epsilon + \frac{p}{p + k_{28}'} - \frac{p}{k_p \tau} - \alpha \frac{p}{k_d + p} \cdot \frac{1}{1 + \frac{p}{k_{comp}}}] \quad (38)$$

with the main difference from eq. (35) being the inhibition term, which vanishes for high activator concentration due to competition over RNA polymerase.

The effective reaction-diffusion equation for the activator is thus,

$$\partial_t p_i = D \frac{(p_{i-1} + p_{i+1} - 2p_i)}{L_2^2} - \frac{p_i}{\tau} + f(p_i) \quad (39)$$

$$f(p_i) = \frac{1}{\alpha} \cdot \left(\epsilon + \frac{p_i}{p_i + k_{28}'}\right) - k_I \frac{p_i}{k_d + p_i} \cdot \frac{1}{1 + \frac{p_i}{k_{comp}}} \quad (40)$$

The resulting response function $f(p_i)$ is a minimal model for the gene network dynamics, and shows both monostable and bistable regimes in the phase plane of gene ratio α and lifetime τ, which are consistent with the experiment (Fig. 2A, S6).

The propagator velocity

Traveling fronts and waves emerge in excitable non-linear systems, and are thus expected in the DNA compartment array with a reaction diffusion equation $\partial_t p = D\nabla^2 p + g(p)$ and an autocatalytic nonlinear function $g(p)$. Traveling fronts change the state of the system from its initial state p_{Low} to a state p_{High}. An analytically solvable model is the Fisher-KPP equation[17,46] in which the state p_{Low} is an unstable fixed point and state p_{High} is stable fixed point.

$$\begin{gathered} g(p) \approx k(p - p_{Low}) + o(p^2) \\ g(p_{Low}) = g(p_{High}) = 0 \\ k = \partial_p g(p_{Low}) > 0; \partial_p g(p_{High}) < 0 \end{gathered} \quad (41)$$

In this model a linear analysis is sufficient to deduce a constraint on the front velocity[17,46],

$$v \geq 2\sqrt{kD}, \quad (42)$$

where $k = \partial_p g(p_{LOW})$ is the rate constant of the autocatalytic process and D is the diffusion coefficient. Indeed, this condition was experimentally observed in BZ reactions[16] as well as in more recent DNA autocatalytic reactions[14].

Another class of models which exhibit front propagation are bistable systems[18,47,48], in which both the initial and final states of the system are stable fixed points, and an additional unstable fixed point $p_{Low} < p_{TH} < p_{High}$,

$$\begin{gathered} g(p_{LOW}) = g(p_{TH}) = g(p_{HIGH}) = 0 \\ \partial_p g(p_{LOW}), \partial_p g(p_{HIGH}) < 0 \end{gathered} \quad (43)$$

DOI: 10.1038/NPHYS3469

A bistable system is more robust to external perturbations and thus offers an experimental advantage for studying front propagation. At a higher level of complexity appear the FitzHugh-Nagumo (FN) and Hodgkin-Huxley (HH) type models, which are characterized with traveling pulses solutions. In bistable systems, FN and HH systems linear analysis around the initial state p_{LOW} does not provide information about the front velocity, but there are other velocity constraints that include integration over the entire function $g(p)$[49].

In addition, we expect a scaling relation based on dimensional analysis[50],

$$v \propto \sqrt{kD}. \tag{44}$$

Here k is a suprathreshold excitation rate, which may be a complex function of the system's kinetic parameters and can be extracted experimentally[16]. In our system the effective diffusion coefficient is $D = 0.021\text{mm}^2\text{hr}^{-1}$ and the measured growth rate of the autocatalytic process is $k = 5.4hr^{-1}$(Fig. S5). Thus, the predicted velocity is 0.33mm/hr close to measured velocities, $v = 0.2 - 0.62$mm/hr.

Flow in the compartment array

The capillaries connecting the 1D array were parallel to the flow channel hence a pressure drop was maintained along the array. But flow in the array was minimized because of its high hydrodynamic resistivity compared to that of the flow channel, The shallow $h \approx 2\mu$m and thin $W_c = 10\mu$m capillaries were whereas the main flow channel was deep H$\approx 50\mu$m and wide $W_m = 900\mu$m. The flow rate in the main flow channel was set to $Q = 0.2\mu$l/min, yielding a mean velocity in the main channel of $v = 180$mm/hr. The ratio between the flow velocity in the capillaries and the main channel is estimated by,

$$\frac{v_{capillary}}{v_{main}} = \frac{\mathrm{R_m A_m}}{R_c A_c} = \left(\frac{L_m}{L_c}\right)\left(\frac{h_c}{h_m}\right)^2 \approx 2 \cdot 10^{-4}. \tag{45}$$

Here we used the Poiseuille equation for hydrodynamic resistance in a rectangular cross section, $R = \frac{12\eta L}{h^3 W}$, with CFE viscosity is η. We neglected the dimensions of the compartment and treated it as a point along the capillary array. Thus, the velocity in the capillary connecting the compartments was $v_{capillary} = 0.036$mm/hr. Finally, we compare the protein diffusion time τ_{Diff} between compartments of length $L = 0.4$mm, to the flow time τ_{flow} :

$$\begin{aligned} \tau_{flow} &= \frac{L}{v_{flow}} \approx 11\text{hr}, \\ \tau_{diff} &= \frac{L^2}{2D_0} \approx 0.6\text{ hr}, \end{aligned} \tag{46}$$

concluding that indeed transport by diffusion was dominant, $\tau_{diff} \ll \tau_{flow}$.

Variation in DNA Ratio and compartment lifetime

To determine the variation in gene ratio between compartments, we analyzed the variation in total DNA density. We measured the fluorescent intensity of the end labeled DNA in a series of compartments. All three DNA segments were end-labeled with a red fluorophore (647nm), the inhibitor the autocatalytic constructs and the reporter. The variation was measured for 196 DNA compartments in 14 sets of 14 different concentrations normalized to their mean fluorescence, the mean variation was found to be $\Delta\alpha = 12\% \pm 3\%$ (Fig. S7,a).

The lifetime in the compartment is set by the geometrical parameters, which are patterned by lithography $\tau \propto R^2 L/W$, where R is the compartment radius L is the capillary length and W is the capillary width. The variation due to local differences in fabrication is estimated from image analysis of geometrical parameters. The ratio $R^2 L/W$ was measured for 214 compartments in two separate devices. The variation in lifetime was found to be $\Delta\tau = 8\%$(Fig. S7, b).

Analysis of the propagation velocity

For each compartment in an array with a given gene ratio α a time derivative of the protein concentration was calculated

$$\frac{dp}{dt} = \frac{p_{i+1} - p_i}{\delta t},$$

where p_i is the protein level at frame i, and δt is the time difference between measurements (Fig. S14). The time derivative dynamics at each compartment is characterized by a peak at the time of arrival of the propagating front. Thus, we set the compartment onset time as the time at which the derivative reached its maximal value. The velocity and its error were calculated from the slope of the compartment as a function of its onset time $x(\tau_{on})$ (Fig. S14b).

DOI: 10.1038/NPHYS3469

Bibliography

46. Kolmogorov, A., Petrovsky, L. & Piskunov, N. An investigation of the diffusion equation combined with an increase in mass and its application to a biological problem. *Bull Uni Moscow Ser Int A* **1,** 1–26 (1937).

47. Marsden, S., Wiggins, L. & Glass, L. *Interdisciplinary Applied Mathematics. Mathematical physiology*. (1993).

48. Volpert, V. & Petrovskii, S. Reaction-diffusion waves in biology. *Phys. Life Rev.* **6,** 267–310 (2009).

49. Benguria, R. D. & Depassier, M. C. Speed of Fronts of the Reaction-Diffusion Equation. *Phys. Rev. Lett.* **77,** 1171–1173 (1996).

50. Luther.R.Z. Investigation and analysis of chemical waves. *Elektrochem.* **12,** 596 (1906).

51. Showalter, K. & Tyson, J. J. Luther's 1906 discovery and analysis of chemical waves. *J. Chem. Educ.* **64,** 742 (1987).

52. Tomchik, K. J. & Devreotes, P. N. Adenosine 3',5'-monophosphate waves in Dictyostelium discoideum: a demonstration by isotope dilution--fluorography. *Science* **212,** 443–6 (1981).

53. Jaffe, L. F. Organization of early development by calcium patterns. *Bioessays* **21,** 657–67 (1999).

54. Yu, S. R. *et al.* Fgf8 morphogen gradient forms by a source-sink mechanism with freely diffusing molecules. *Nature* **461,** 533–6 (2009).

55. Müller, P., Rogers, K. W., Yu, S. R., Brand, M. & Schier, A. F. Morphogen transport. *Development* **140,** 1621–38 (2013).

56. Maeda, H., Fujita, N. & Ishihama, A. Competition among seven Escherichia coli sigma subunits: relative binding affinities to the core RNA polymerase. *Nucleic Acids Res.* **28,** 3497–503 (2000).

57. Chadsey, M. S., Karlinsey, J. E. & Hughes, K. T. The flagellar anti-sigma factor FlgM actively dissociates Salmonella typhimurium sigma28 RNA polymerase holoenzyme. *Genes Dev.* **12,** 3123–36 (1998).

Figures

Main Text

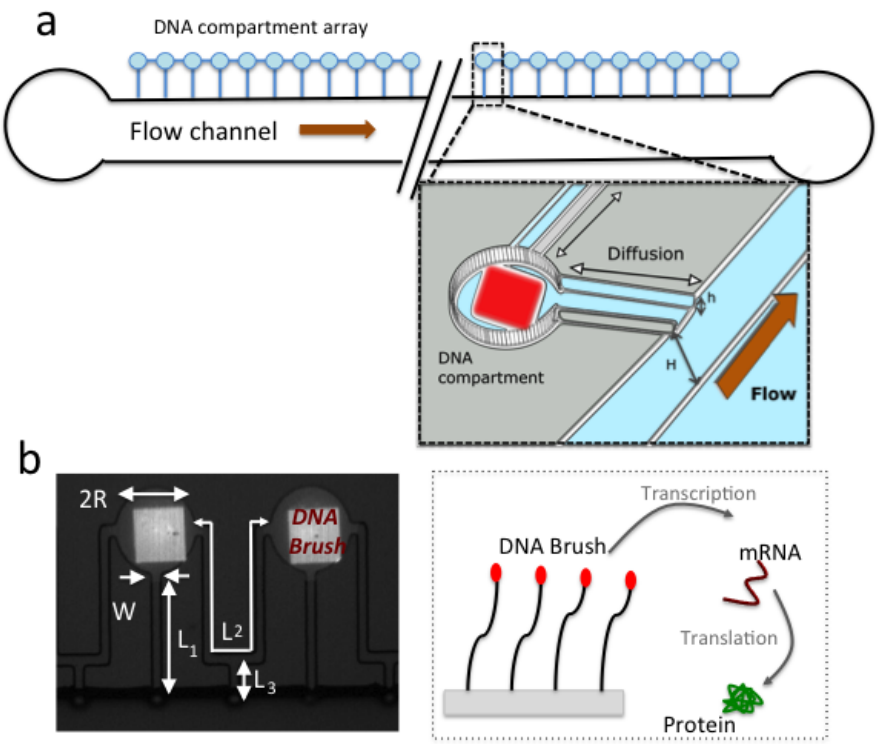

Fig. S1. Microfluidic device and DNA compartment array.

(a) An array of circular compartments carved in silicon (h~2μm) and connected through small capillaries to a flow channel (H~50μm). Each compartment is patterned with a DNA brush. The transcription/translation cell extract enters by diffusion into the thin capillaries from the flow channel. **(b)** Image of end labeled DNA brush (white square, red fluorophore, 647nm). Compartment dimensions $R = 50\mu m, L_1 = 150\mu m, L_2 = 400\mu m, L_3 = 40\mu m$ and $W = 12\mu m$. In the compartments, proteins are expressed from the brush and diffuse through the capillaries.

DOI: 10.1038/NPHYS3469

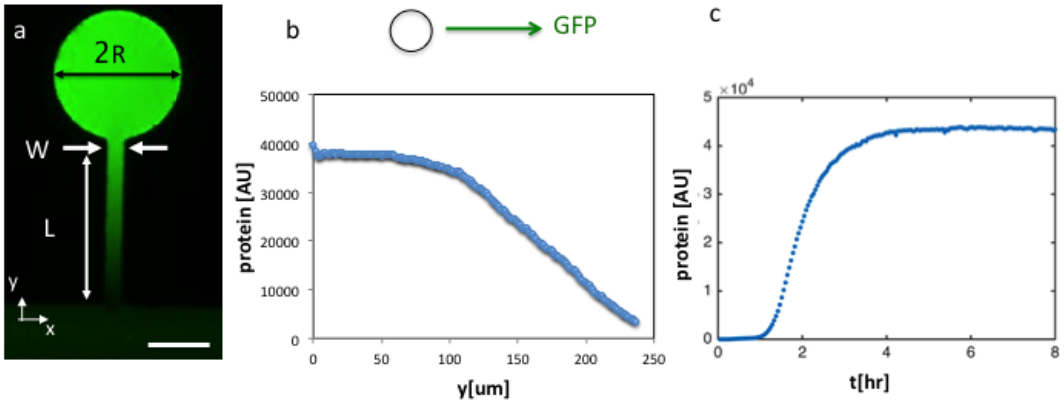

Fig. S2. Linear concentration profile along the capillary in a single compartment

(a) Fluorescent image of a single compartment patterned with an unregulated gene constitutively expressing GFP. Compartment dimensions radius $R = 50\mu m$, capillary length $L = 150\mu m$, capillary width $W = 12\mu m$ and height $h = 2.5\mu m$. Scale bar 50μm. (b) GFP concentration profile for an unregulated construct along the compartment and capillary. The profile is homogenous in the compartment and decays linearly from a maximal value in the compartment to zero value at the flow channel. (c) Protein expression kinetics in the compartment reaching a steady-state level and running for 8 hours

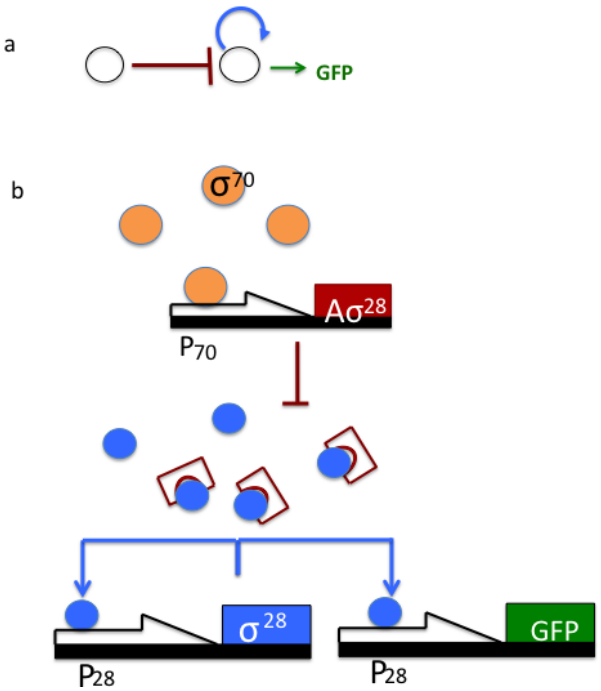

Fig. S3. Bistable gene circuit network scheme.

(a) Network scheme of an Inhibitor-Autocatalytic construct with a GFP reporter. **(b)** An autocatalytic construct with transcription factor σ^{28} activating its own promoter and activating a reporter construct synthesizing GFP. The positive feedback of the autocatalytic construct is inhibited by $A\sigma^{28}$ protein binding to the σ^{28}, preventing it from binding to the P_{28} promoter.

DOI: 10.1038/NPHYS3469

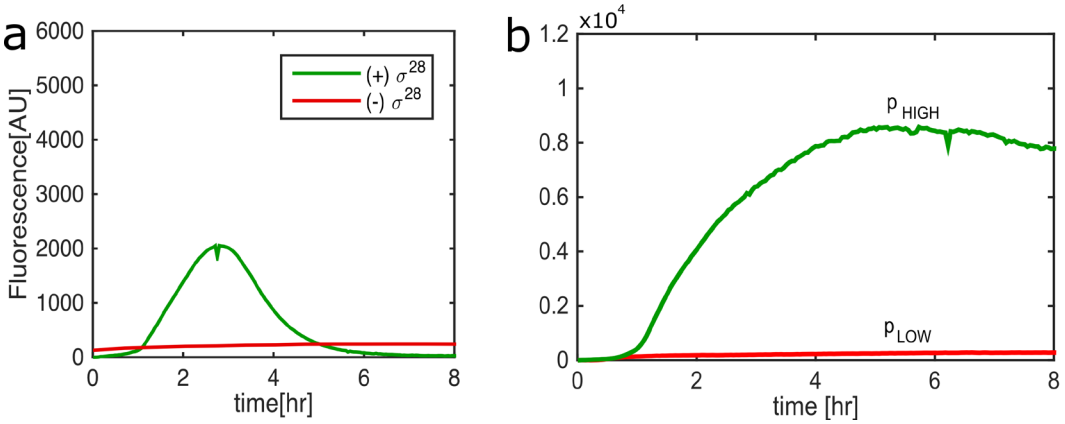

Fig. S4. The bistable protein kinetics.

(a) A reporter gene, with inhibitor concentration of 100nM, without an autocatalytic element, responding to an external addition of σ^{28} transcription factor (t<3.5hr), and shutting down expression when external signal is washed out of the system (t>3.5hr) (green) reporter gene with no external addition of σ^{28} transcription factor(Red). Measurements conducted in two different experiments. **(b)** A bistable construct in a single compartment responding to the external perturbation of σ^{28} transcription factor. The compartment switches to high expression levels p_{HIGH} as a result of the perturbation. In the absence of the perturbation low expression levels p_{LOW} is maintained. The bistable construct was taken with $\alpha = 1.6, \tau = 0.9$hr.

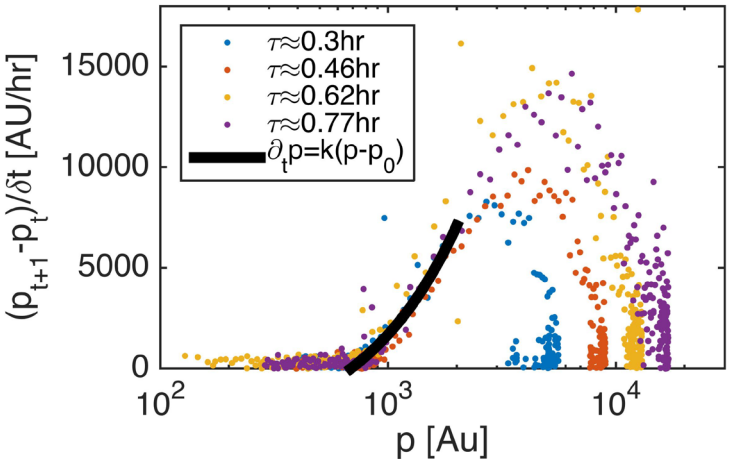

Fig. S5. Growth rate of the autocatalytic process *k*.

Protein derivative in $[\mathrm{AU} \cdot \mathrm{hr}^{-1}]$ as a function of protein concentration in AU . Black line is a linear fit with a slope of $k = (5.4 \pm 1)\mathrm{hr}^{-1}$.

DOI: 10.1038/NPHYS3469

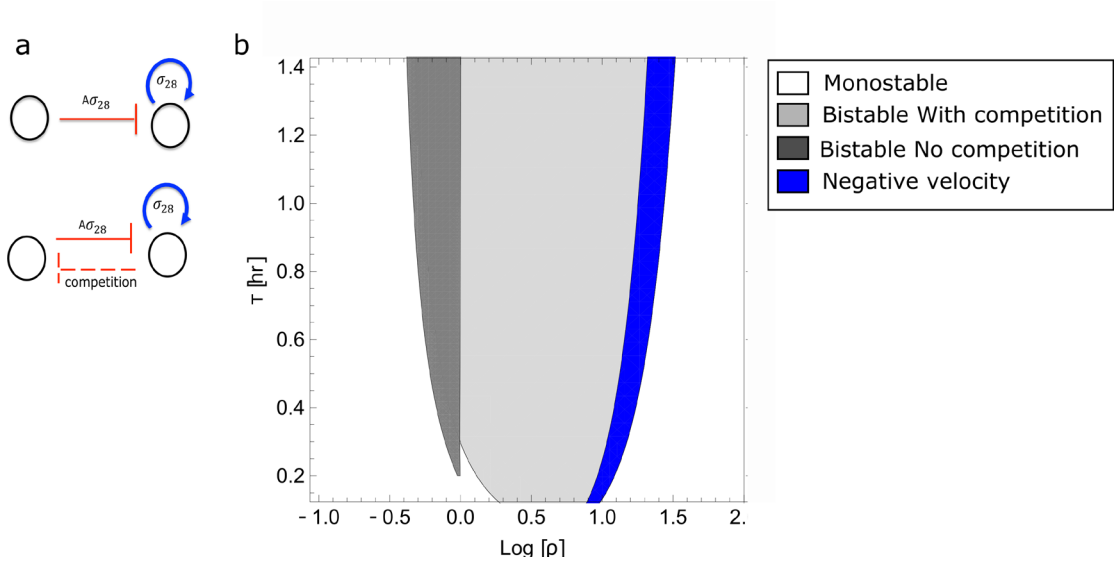

Fig. S6. Phase diagram with and without competition over RNAP.

(a) Network scheme without competition over RNAP and with competition. **(b)** Phase diagram of the monostable (White) and bistable regions without competition (Dark Gray) with competition (Bright gray) and a region corresponding to theoretical negative velocity (Blue)

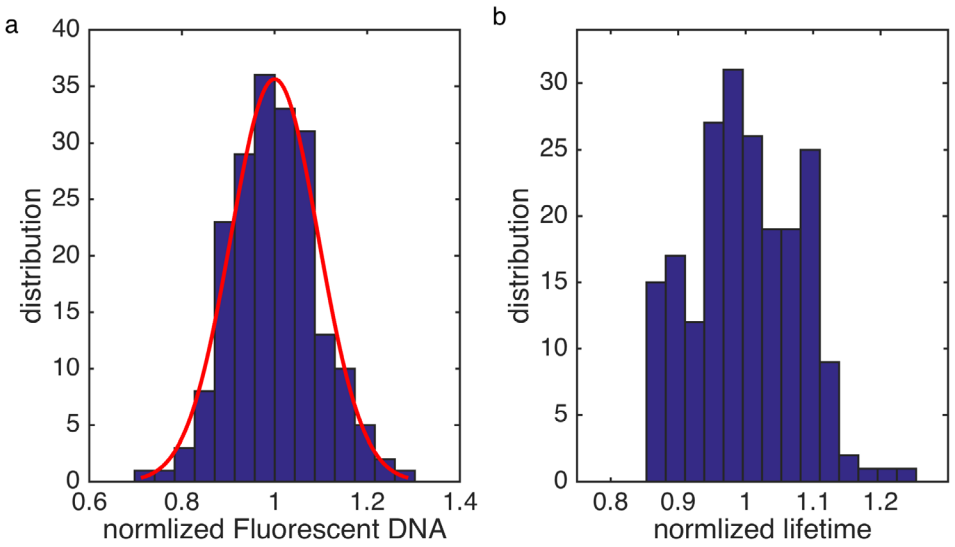

Fig. S7. Variation in DNA ratio, α, and compartment lifetime, τ.

(a) Distribution of 196 measurements of fluorescence end labeled DNA (647nm). 14 different gene ratios normalized to their mean fluorescent value in 14 different compartments. Red line is a fit to a Gaussian with an expected value $\mu_{DNA} = 0.99$ of normalized fluorescent DNA and variance $\sigma_{DNA}^2 = 0.016$ normalized fluorescent DNA, compatible to a variation of $12 \pm 3\%$. (b) Distribution of 214 normalized geometrically calculated lifetimes, $\tau \propto \frac{R^2 L}{W}$, calculated from image analysis of dimensions of compartments. Variation is due fabrication differences. Data is taken for two separate chips. Variation in data is $\Delta\tau = 10\%$.

DOI: 10.1038/NPHYS3469

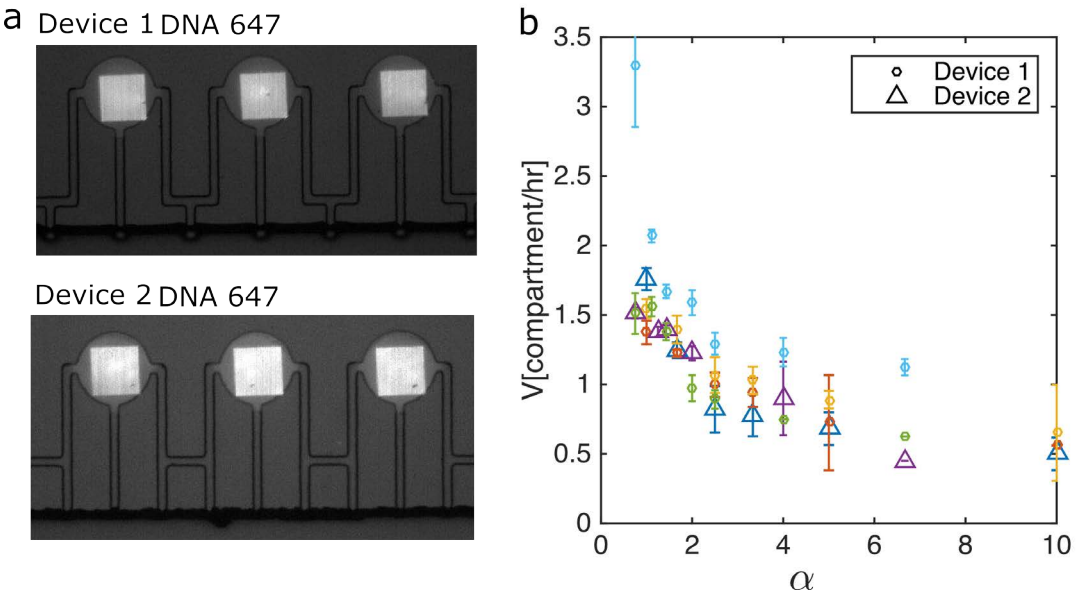

Fig. S8. Propagation velocity for different experiments.

(a) DNA brush patterned in two array geometries. Both have effective lifetime of $\tau \sim 0.4$hr **(b)** Propagation velocity in [compartment/hr] as measured as a function of gene ratio. Different colors indicate different experiments. Measurements are taken both from device 1 (circles) and device 2 (triangles).

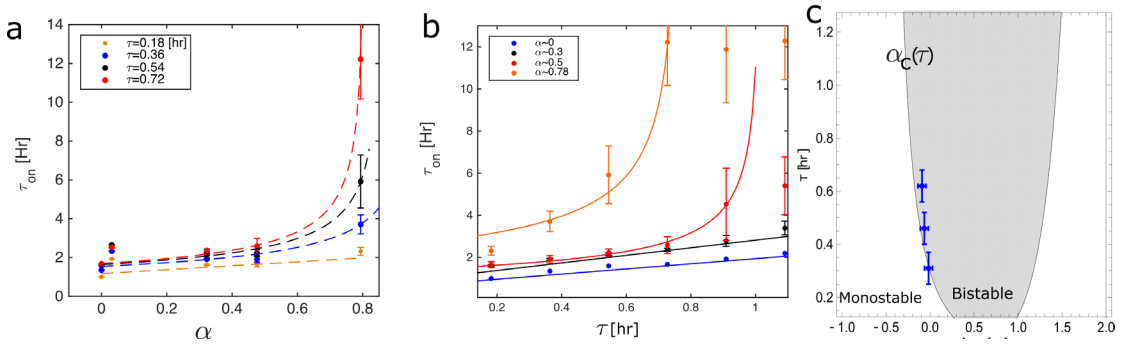

Fig. S9. Divergence of onset times near the transition.

Onset time τ_{on} of the bistable gene circuit in single compartments as a function of **(a)** gene ratio $\alpha = \frac{G_I}{G_A}$ at four different lifetime values τ, each corresponding to a different critical value of gene ratio, α_c. Dashed lines are fits to power laws, $\tau_{on} = \tau_0(\alpha - \alpha_c)^{-\frac{1}{2}}$ **(b)** Protein lifetime in the compartment τ, at four different gene ratios. Data points that do not fit the line include onset times that are larger than the measurement time and therefore relate only to the lower limit of the measurement. Each point is an average over 9 measurements. Solid lines are fits to power law $\tau = \tau_0\,(\tau - \tau_c)^{-\frac{1}{2}}$.**(c)** Three points $\alpha_c(\tau)$ from the fit to the lines in (a) plotted on the phase diagram.

DOI: 10.1038/NPHYS3469

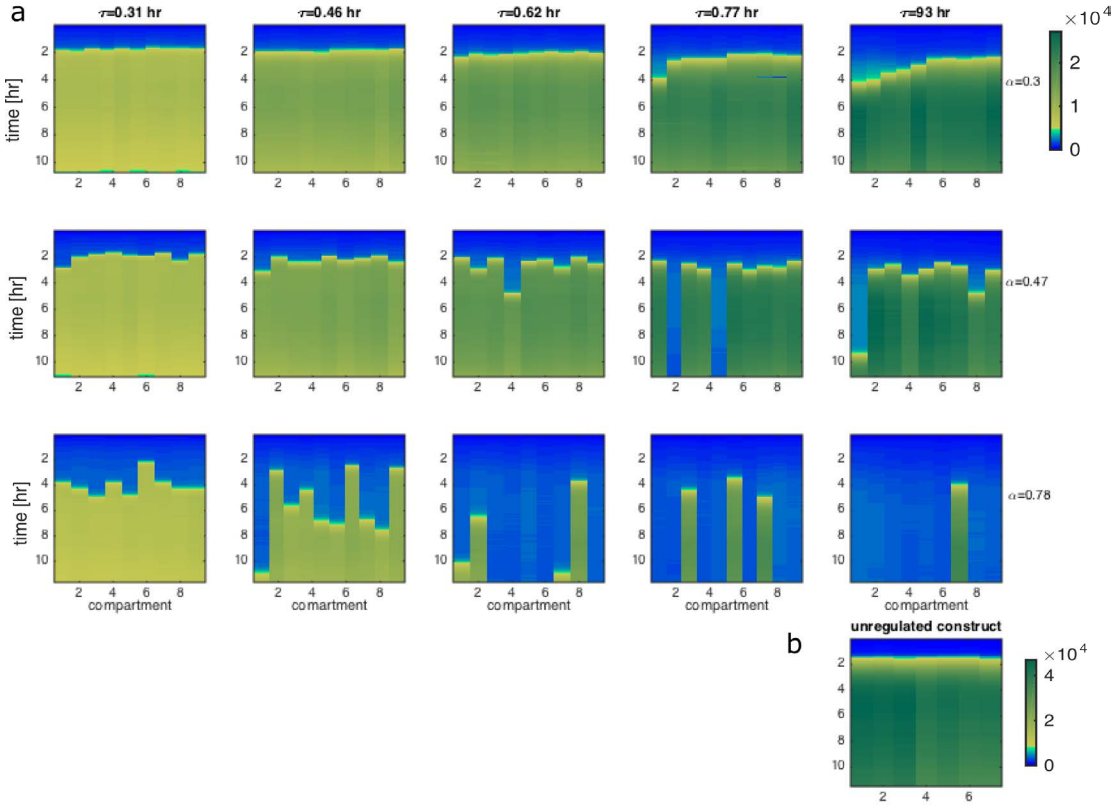

Fig. S10. Onset time in single compartments for different gene ratios and lifetimes approaching the transition to the bistable regime.

(a) Space time plots of single compartments patterned with the bistable gene circuit at different gene ratios $\alpha = 0.3 - 0.78$ and lifetimes $\tau = 0.3 - 0.93$hr. Experiment was conducted by varying the length of the capillaries $L = 100 - 300$μm. Each plot consists of 9 identical single compartments. High (Low) expression state p_{HIGH} (p_{LOW}) marked in green (blue). Shades of green correspond to different levels of expression for by different concentration of sigma-28, as noted in the color bar. **(b)** Space time plot for an unregulated construct expressing GFP under a P_{70} promoter at lifetime $\tau = 0.93$hr. Plot consists of 7 identical single compartments. Variation between expression times is about 5%.

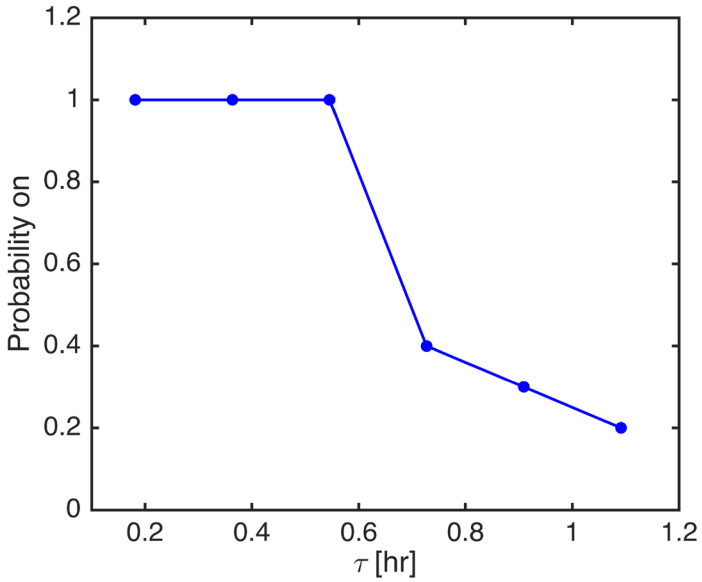

Fig. S11. Probability to switch into an active state near the transition.

Number of compartments with high expression levels divided by number of compartment in the experiment at a given lifetime τ. Nine measurements were conducted for every τ. All measurements are for gene ratio $\alpha = 0.78$.

DOI: 10.1038/NPHYS3469

SI Figures

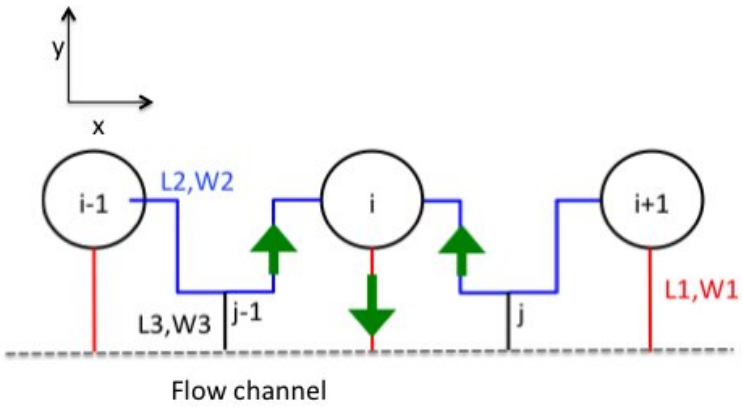

Fig. S12. DNA compartment scheme

Illustration of compartments array interconnected by capillaries with a short shunt to the main flow channel Synthesized protein diffuses along the x-axis to adjacent compartments and along the y-axis to the main channel to be evacuated from the array.

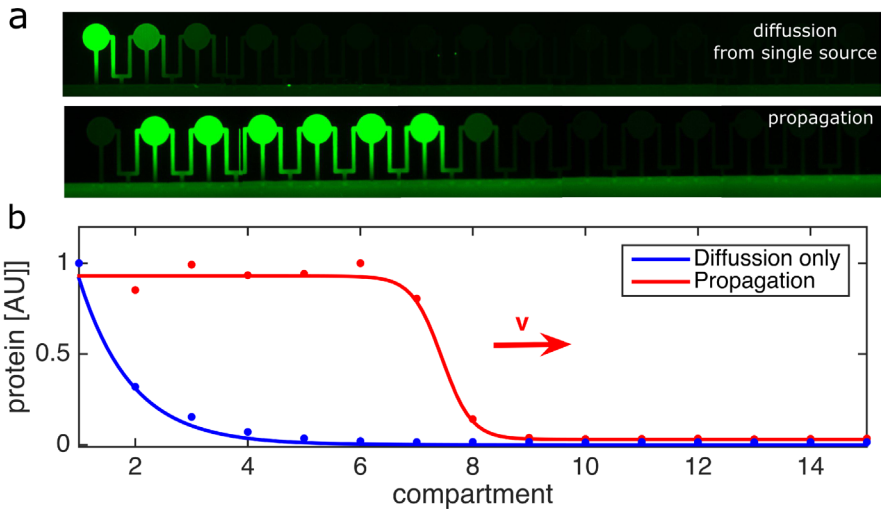

Fig. S13. Single-compartment exponentially decaying profile and propagating front in array.

(a) Image of GFP expression profile along the DNA array generated from a source is located in the leftmost compartment. The GFP intensity is homogenous within a compartment, decays between two neighboring compartments image taken at $t = 4$hr. Second image, GFP expression profile propagating along the array at $t = 6$hr. **(b)** Protein profile along the array for a single DNA source (Blue), and propagator network (Red).

DOI: 10.1038/NPHYS3469

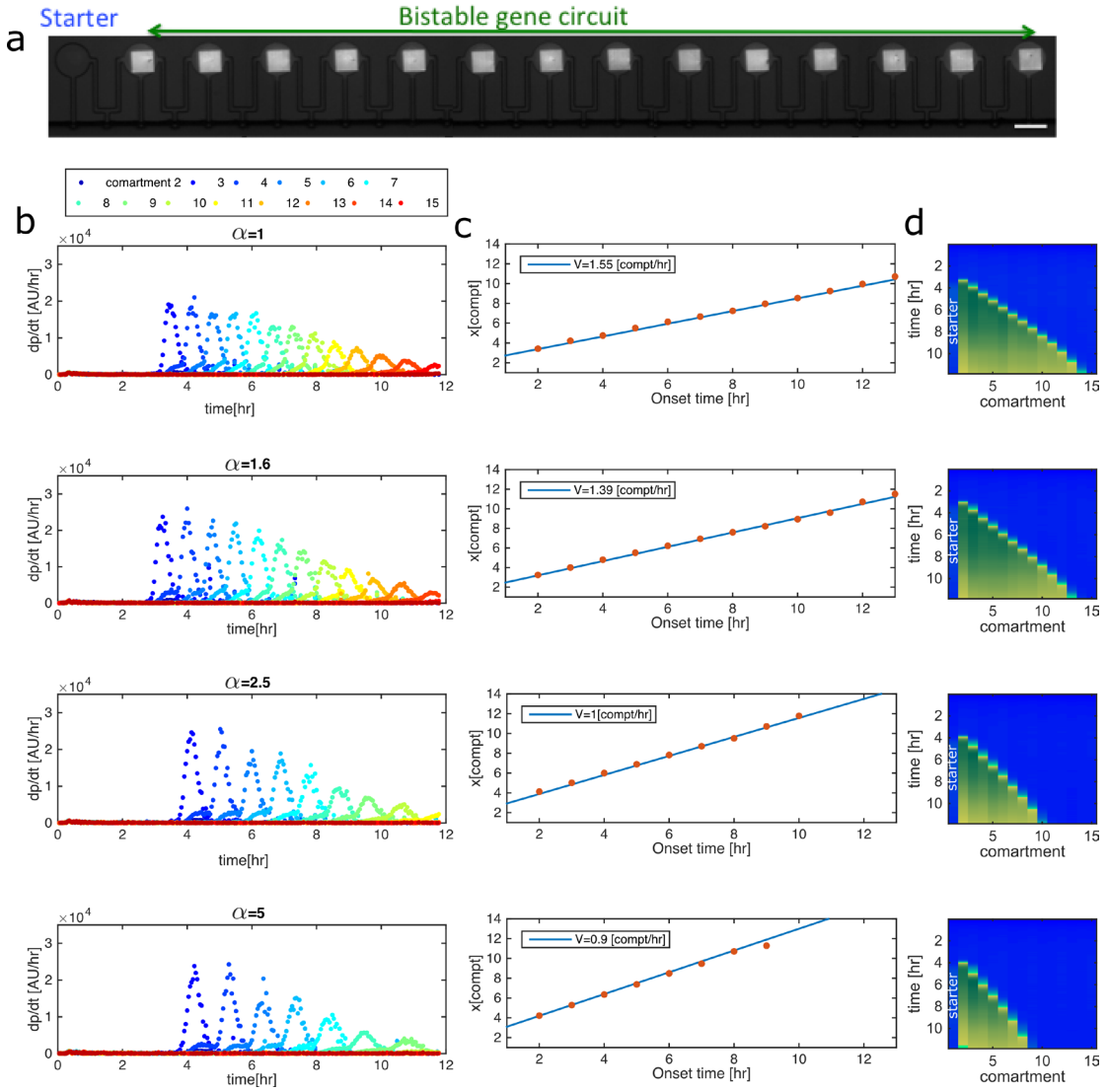

Fig. S14. Time derivative of protein concentration and velocity measurements.

(a) DNA Brushes in an array of 15 connected compartments: the leftmost compartment patterned with a low-density starter amount of activator, and compartments 2-15 patterned with the bistable gene circuit. Measurement are plotted for lifetime $\tau = 0.4hr$ and varying gene ratio, $\alpha = 1, 1.6, 2.5, 5$. **(b)** Plots of time derivatives of protein synthesis kinetics in compartments. **(c)** Distance from origin as a function of compartment onset time, with propagation velocity evaluated from the slope. **(d)** Space-Time plot of propagator, Low (High) expression levels are marked in Blue (Green).

Model System	Signal	Velocity [mm/hr]	$k[\mathrm{hr}^{-1}]$	D $[\mathrm{mm}^2/\mathrm{hr}]$	$\sqrt{D/\tau}$ [mm /hr]
Neurons (Squid Giant Axon)[51]	Action Potentials	$4 \cdot 10^7$	$3.6 \cdot 10^6$	$3.6 \cdot 10^7$	10^7
Heart (Myocytes guinea pig)[28]	Calcium Waves	360	22,320	2.52	237
Belousov Zhabotinsky reaction[16]	Chemical weves	144	720	7.2	72
Dictyestilum[28,52,53]	cAMP Waves	18	21	4	9
Xenophus [11]	Mitosis Waves	3.6	36-360	0.036	1-3.6
In vitro enzymatic catalytic reaction[14]	DNA	3.6	4.68	0.3	1.1
DNA compartments (present work)	Gene expression	0.62	5.4	0.21	0.33
Somitogenesis (Zebra fish values taken from FGF8)[26,54,55]	Gene expression	0.072	5.7	0.0057 ± 0.0072	0.018

Table S1. Luther scaling – propagation velocities, diffusion coefficients, and reaction rates in different systems.

DOI: 10.1038/NPHYS3469

Promoter	Description	Reference
P_{70}	Lambda phage promoter OR2-OR1-Pr specific to E. coli σ^{70}.	36
P_{28}	Promoter of the tar gene (E. coli) specific to σ^{28}	37
Untranslated region		
UTR1	The untranslated region containing the T7 g10 leader sequence for highly efficient translation initiation	37
Transcription terminator		
T500	Transcription terminator for E. coli RNA polymerase	37
Gene		
GFP	The enhanced green fluorescent protein truncated and modified in N- and C- termini.	37
σ^{28}	rpoF (E. coli σ^{28})	37
$A\sigma^{28}$	Anti-sigma factor FlgM (E. coli Aσ^{28})	45

Table S2. DNA Modules

	Description	
Network 1	Autocatalytic	$P_{28} - \sigma^{28}$
	Inhibitor	$P_{70} - A\sigma^{28}$
	Reporter	$P_{28} - deGFP$
Starter		$P_{70} - \sigma^{28}$

Table S3. DNA Constructs – Bistable network and starter.

	REF	Parameter	Value
σ^{28} Synthesis rate	13	k_I	$1-2\mu M/hr$
Leak of the p_{28} promoter		ϵ	1-10%
Michaelis-Menten constant binding of σ^{28} to the promoter P_{28}.	56	k_{28}	$0.74-2.96nM$
Effective binding affinity of the sigma – anti-sigma		$k_d = \frac{k_{off}+1/\tau}{k_{on}}$	
On and off rates of binding of $A\sigma-\sigma^{28}$ proteins	57	$\frac{k_{off}}{k_{on}}$	$0.1-0.2nM.$
The affinity constant nM is proportional to the σ^{70} concentration in the extract	29,37	k_{comp}	0.8nM*

Table S4. Values taken for the rate balance plots and the phase diagram.

*number taken lower than the value in literature

DOI: 10.1038/NPHYS3469

Video

Propagating gene expression front. Bistable circuit dynamics imaged by GFP propagating along a 1D array of DNA compartments. One sec in the video corresponds to 66min in the experiment.